*The Aeronautical Journal* (2023), 1–28
doi:10.1017/aer.2023.87

ROYAL AERONAUTICAL SOCIETY

REGULAR PAPER

# Full envelope nonlinear flight controller design for a novel electric VTOL (eVTOL) air taxi

E.C. Suiçmez and A.T. Kutay

Aerospace Engineering, Middle East Technical University, Ankara, 06800, Turkey
**Corresponding author:** E.C. Suiçmez; Email: emrecansuicmez@gmail.com

**Received:** 3 August 2022; **Revised:** 20 July 2023; **Accepted:** 29 August 2023

**Keywords:** incremental nonlinear dynamic inversion (INDI); control allocation (CA); actuator saturation; thrust vector control; distributed electric propulsion (DEP); vertical takeoff and landing (VTOL); air-taxi; urban air mobility (UAM)

## Abstract

On-demand urban air transportation gains popularity in recent years with the introduction of the electric VTOL (eVTOL) aircraft concept. There is an emerging interest in short/medium range eVTOL air taxi considering the critical advantages of electric propulsion (i.e. low noise and carbon emission). Using several electric propulsion systems (distributed electric propulsion (DEP)) has further advantages such as improved redundancy. However, flight controller design becomes more challenging due to highly over-actuated and coupled dynamics. This study defines and resolves flight control problems of a novel DEP eVTOL air taxi. The aircraft has a fixed-wing surface to have aerodynamically efficient cruise flight, and uses only tilting electric propulsion units to achieve full envelope flight control via pure thrust vector control. The aircraft does not have conventional control surfaces such as aileron, rudder or elevator. Using pure thrust vector control has some design benefits, but the control problem becomes more challenging due to the over-actuated and highly coupled dynamics (especially in transition flight). A preliminary flight dynamics model is obtained considering the dominant effects at hover and high-speed forward flight. Hover and forward flight models are blended to simulate the transition dynamics. Two central challenges regarding the flight control are significant nonlinearities in aircraft dynamics during the transition and proper allocation of the thrust vector control specifically in limited control authority (actuator saturation). The former challenge is resolved via designing a sensor-based incremental nonlinear dynamic inversion (INDI) controller to have a single/unified controller covering the wide flight envelope. For the latter one, an optimisation-based control allocation (CA) approach is integrated into the INDI controller. CA requires special attention due to the pure thrust vector control's highly coupled dynamics. The controller shows satisfactory performance and disturbance rejection characteristics. Moreover, the CA plays a vital role in guaranteeing stable flight in case of severe actuator saturation.

## Nomenclature

| | |
|---|---|
| $\phi, \theta, \psi$ | Aircraft Roll, Pitch and Yaw Euler Angles |
| $p, q, r$ | Aircraft body angular velocities |
| $u, v, w$ | Aircraft body translational velocities |
| $h$ | Altitude |
| $M, V_{inf}$ | Mach number and Airspeed |
| $\alpha, \beta$ | Angle of attack and Sideslip angle |
| $\gamma$ | Flight path angle |
| $\bar{q}$ | Dynamic pressure |
| $F^b_{aero}, F^b_{prop}$ | Aerodynamic and Propulsion forces in the aircraft body axis |
| $M^b_{aero}, M^b_{prop}$ | Aerodynamic and Propulsion moments in the aircraft body axis |
| $\delta$ | EDF tilt(deflection) angle |
| $rpm, T, Q$ | EDF rpm, thrust and torque |
| $\sigma$ | EDF turn direction |

| | |
|---|---|
| $fl, fr$ | Front-left and Front-right EDF section |
| $wl, wr$ | Wing-left and Wing-right EDF section |
| $T_{cmd}$ | Thrust commanded by the controller |
| $\delta_{cmd}$ | Tilt angle commanded by the controller |
| $T_{act}$ | Thrust generated by the actuators/EDF considering actuator dynamics |
| $\delta_{act}$ | Tilt angle generated by the actuators/EDF considering actuator dynamics |
| $\omega_{n_T}$ | Natural frequency of the thrust actuator dynamics |
| $\varsigma_T$ | Damping coefficient of the thrust actuator dynamics |
| $\omega_{n_\delta}$ | Natural frequency of the tilt angle actuator dynamics |
| $\varsigma_\delta$ | Damping coefficient of the tilt angle actuator dynamics |
| $U$ | Real(physical) control input vector |
| $U_{act}$ | Real(physical) control input vector considering the actuator dynamics |
| $U_{INDI}$ | INDI control input vector |
| $U_{INDI,0}$ | INDI control input vector at the previous time step |
| $\Delta U_{INDI}$ | Incremental INDI control input vector |
| $\upsilon_{INDI}$ | Virtual INDI control input vector |
| $\Delta\upsilon_{INDI}$ | Incremental virtual INDI control input vector |
| $T_{v,INDI}$ | Transformation matrix between the virtual and INDI control input vectors |
| $x$ | State vector |
| $\dot{x}_0$ | INDI controller's state derivative estimation via sensor measurements |
| $\dot{x}_{req}$ | INDI controller's required state derivatives |
| $T_x$ | Component of thrust in the aircraft body x-axis |
| $T_z$ | Component of thrust in the aircraft body z-axis |
| $g$ | INDI controller's virtual control input matrix |
| $H_f$ | INDI controller noise filter |
| $\omega_{n_f}$ | Natural frequency of the INDI controller's noise filter |
| $\varsigma_f$ | Damping coefficient of the INDI controller's noise filter |
| $\Delta U_{CA}$ | Incremental control input generated by the Control Allocation (CA) algorithm |
| $W_v$ | State weight matrix of the CA algorithm |
| $W_u$ | Control input weight matrix of the CA algorithm |
| $\Delta U_{des}$ | Desired control input increment of the CA algorithm |
| $\gamma$ | Tuning coefficient of the CA algorithm |

### Subscripts

| | |
|---|---|
| *cmd* | Commanded state |
| *act* | Actuator state |
| *req* | Required state |
| *fl, fr* | Front left and Front right EDF section |
| *wl, wr* | Wing left and Wing right EDF section |

## 1.0 Introduction

In the last decades, a new concept that could shape the future of aviation has emerged with the introduction of the term *On-demand mobility* (ODM) by NASA [1]. On-demand urban air transportation is part of this concept, and there is a growing interest in finding feasible solutions to this problem both in industry and academy. Several reports and studies show the potentials and increasing market share of the on-demand urban air transportation in aviation [2–6]. As stated on most of these reports and studies, two main goals of feasible urban air transportation considering the environmental effects are achieving very low noise and carbon-emission levels. Electric propulsion comes with significant advantages compared to the conventional propulsion systems considering these goals [3, 4, 6].

Moreover, it is possible to use several smaller-sized electric propulsion units in a combined way thanks to the electric propulsion system's design flexibility [7]. DEP refers to propulsion systems with

https://doi.org/10.1017/aer.2023.87 Published online by Cambridge University Press

several electric propulsion units used in a distributed and desired way [8]. DEP can be used as a thrust vector control concept to provide thrust for both vertical takeoff and landing (VTOL) and forward flight. VTOL ability combined with efficient forward/cruise flight is essential to satisfy medium-range urban air transportation requirements [2]. At this point, the combination of DEP with VTOL ability provides a feasible aircraft concept for the on-demand urban air transportation problem [4, 6].

Besides low noise level and zero carbon-emission, the DEP concept has further advantages of increased efficiency and redundancy [4, 6]. Regarding the efficiency, it is crucial to compare electric propulsion with conventional propulsion systems using the metrics that consider the integrated system [3]. Although the exact estimation of the integrated system's overall efficiency is challenging, the expected increase in the DEP system's overall efficiency is significant [3, 6]. The inherent robustness to failures is another critical advantage of DEP thanks to the concept's over-actuated nature. Actuator failures can be handled effectively redistributing the reduced control authority to working actuators/propulsion units.

On the other hand, the electric propulsion's main drawback is the batteries' limited energy storage [3, 4]. Especially for the fixed-wing DEP VTOL air taxi, the power density becomes more critical since a significant amount of power is needed for the vertical flight/VTOL, and the forward flight/cruise requires much less power with the help of the aerodynamic lift. Although current batteries' limited energy and power density is a significant challenge for the DEP VTOL concept, many startup companies have already achieved serious investment for this concept and made successful flights with prototype aircraft [2]. A NASA study also supports that the energy density is already sufficient for some DEP concepts if electric propulsion's feasibility is analysed using the metrics that consider complete integration of the electric propulsion system instead of the conventional propulsion metrics [3]. Another study focuses on the conceptual design and feasibility of a two-seat personal electric VTOL aircraft [9]. It is concluded that the DEP VTOL concept has a great potential to solve the urban air transportation problem in a safe, quiet, environmentally friendly and efficient way.

Significant advantages of the electric propulsion lead many companies to design and build eVTOL aircraft to solve the on-demand urban air transportation problem. Some of the companies with promising eVTOL air taxi projects are Lilium, Volocopter, Joby Aviation, Uber and Ehang. Some of these air taxi projects use both fixed-wing and tilting electric propulsion units to achieve VTOL in combination with efficient forward/cruise flight with the help of fixed-wing aerodynamic surfaces. This solution comes with additional complexity, especially during the transition between hover and high-speed forward flight. However, the benefit gained from a fixed-wing can be significant for longer-range flights. Two main configurations used to achieve the transition are tilt-rotor and tilt-wing concepts. Some of the other configurations are also described in a study with more details [10].

Compared to classical tilt-wing and tilt-rotor concepts, a unique DEP eVTOL air taxi concept is considered in this study. The studied aircraft is inspired by the Lilium jet (see Fig. 1), but it is also noted that the aircraft designed and studied in this paper is different from the Lilium jet. Therefore, all the results and conclusions of the thesis are not related to the Lilium jet.

The Lilium company [11] is build as a startup to find an innovative solution for the urban air transportation. With significant amount of funding in years (around $1 billion), the company grew very fast and became one of the successful pioneers of the eVTOL air taxi projects. Lilium jet has a unique design compared to common eVTOL concepts. It has a fixed-wing surface for efficient high-speed forward flight and several tilting electric ducted fans (EDF) distributed over the wing and canard sections. EDFs are tilted to control thrust vector and achieve the transition between hover and forward flight (Fig. 1). Aircraft do not have any conventional control and stability surfaces such as aileron, elevator, rudder, horizontal/vertical tail, etc. Full envelope flight control is achieved by pure thrust vector control (i.e. adjusting tilt angle and rpm of EDFs). Not having conventional control/stability surfaces has critical advantages: improved aerodynamic efficiency at high-speed forward flight, design flexibility-simplicity, better sizing-weight savings, etc. On the other hand, it also comes with problems/challenges regarding the flight control such as open-loop directional unstability, limited control authority at specific flight conditions, resolving actuator saturation is not straightforward due to the thrust vector couplings, etc.

https://doi.org/10.1017/aer.2023.87 Published online by Cambridge University Press

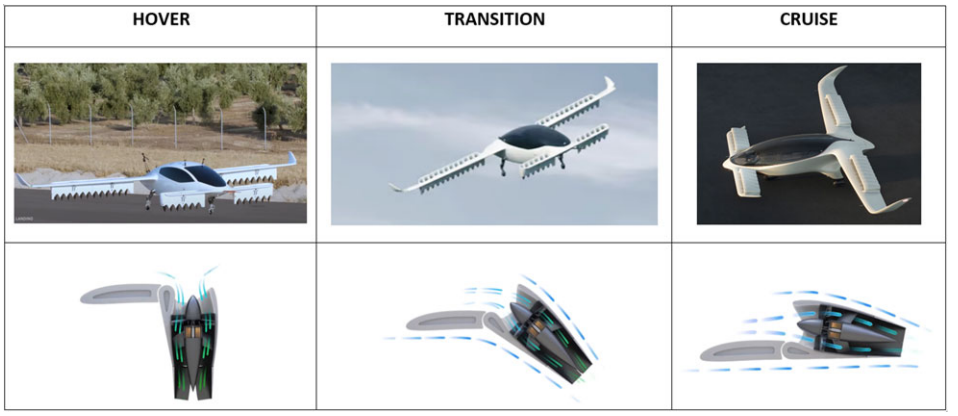


***Figure 1.*** *Lilium-jet photos at hover, transition, cruise flight and corresponding EDF positions [11].*

To sum up, contribution of the study is defining and resolving flight control problems of a unique fixed wing eVTOL aircraft which is not studied previously to the author's knowledge. The designed controller must cover wide flight envelope of the air taxi operation mainly consisting of vertical takeoff, transition from hover to forward flight, forward flight (with climb/descent and turns), transition from forward to hover flight and vertical landing. Moreover, controller must consider actuator saturation problems with specific control allocation design since novel pure thrust vector control has unique problems. The main challenging points for the unified controller design and proposed solutions/contributions are summarised as follows:

- Severe nonlinearities and couplings occur in flight dynamics, especially during the transition region due to the DEP thrust vector dynamics and fixed-wing aerodynamic effects. A nonlinear dynamic inversion-based controller approach, INDI is adapted to the problem to effectively handle nonlinearities/couplings. INDI reduces dependency on the aircraft model significantly while performing the dynamic inversion since it replaces the model information with the sensor data. Thanks to the sensor-based dynamic inversion, the model dependency of the designed INDI controller is only mass, inertia and EDF lever-arm (mainly depending on the geometry) information (see Section 3.2). This property of INDI makes it a good candidate to control the hard-to-model highly nonlinear flight dynamics of this novel air taxi concept, especially considering the transition flight. INDI is formulated to have a unified controller structure that covers the entire flight envelope. Literature review and formulation of the INDI controller are given in Sections 3 and 3.2, respectively.
- Control of the air taxi is achieved by pure thrust vector control (i.e. adjusting the rotor speed/revolutions per minute (rpm) and tilt angle) of several EDFs, and there are no conventional control surfaces. The system is over-actuated (five control axis and eight control effectors, see Section 3.1 for details) and it is crucial to distribute the limited control authority effectively in case of actuator saturation. If the actuator saturation is not adequately considered in the design, then the controller will be ineffective, and instability can occur (see Section 4.4). Formulating a direct relation between control channels/axis and control effectors/actuators is not straightforward due to the coupled nature of the pure thrust vector control. Therefore, standard saturation resolving approaches used in conventional aircraft (e.g. anti-windup) is not straightforward to implement. An optimisation-based CA method is integrated into the INDI controller considering these points. The CA prioritises rotational channels over translational channels to allocate the limited control authority such that the stability of the aircraft is guaranteed. The integration of the CA to the INDI controller requires specific attention due to the thrust vector control's coupled nature. Literature review and design of the CA are given in Sections 3 and 3.3, respectively.

https://doi.org/10.1017/aer.2023.87 Published online by Cambridge University Press

In literature, there are few studies regarding the full envelope flight control of fixed-wing eVTOL aircraft similar to the one studied in this paper. In Ref. (12), a novel fixed-wing tilt-rotor UAV is modeled, and an INDI-based flight controller is designed for the full flight envelope. The authors describe the challenges experienced in transition due to the strong nonlinearities in the aerodynamic model and the couplings introduced by the thrust vector control. The study shows that the INDI-based controller gives satisfactory results but need further investigations to analyse the robustness and disturbance rejection properties. Another study focus on the control of a quad tilt-rotor eVTOL with conventional aerodynamic surfaces [13]. An INDI-based controller is designed in combination with CA approaches to have a unified controller. Results show that the INDI-based controller gives satisfactory performance for the entire flight envelope. In Ref. (14), a robust full envelope controller is designed for a fixed-wing eVTOL, and the controller is tested considering the robustness measures. The aircraft has conventional control surfaces combined with tilt rotor electric propulsion system. The study does not cover the actuator saturation-related control allocation problems although the aircraft is over-actuated. In another study [15], trajectory tracking of a winged eVTOL aircraft is considered. The study focus on optimisation of pitch and thrust allocation, and high angle-of attack dynamics are considered in the optimisation. Designed controller is more like an outer loop control that generates desired rates for optimal trajectory tracking. The above-mentioned studies use conventional control and stability surfaces (i.e. aileron, elevator, rudder, vertical/horizontal tail, etc.) combined with tilt-rotor propulsion units. The air taxi studied in this paper differentiates from the other fixed-wing eVTOL concepts since using only tilt rotor units (i.e. pure thrust vector control) to achieve full envelope flight control. As mentioned previously, this is a significant advantage regarding simplicity, sizing and aerodynamic efficiency but comes with additional challenges/problems for the flight control such as open-loop directional instability in forward flight due to tailless design (see Section 2.1), hard to resolve actuator saturation-related problems due to highly coupled pure thrust vector control (see Section 3).

To conclude, this study's main contribution is defining and resolving the challenges of a novel fixed wing eVTOL air taxi that has not been studied before, to the author's knowledge. The aircraft is unique so that there are no aerodynamic and propulsion models to simulate the flight dynamics. Therefore, the first part of the study focuses on generating preliminary aerodynamic and propulsion models. The aim of this study is not generating a high-fidelity flight dynamics model but considering the main aerodynamic and propulsion effects to simulate the air taxi for the full-flight envelope. The main focus and contribution of the study are designing an unified flight controller, which effectively resolves the flight-control-related problems/challenges described earlier. INDI approach is combined with CA methods to design the unified flight controller. The detailed introduction and literature survey of INDI and CA methods are specifically given in Section 3.

## 2.0 Flight dynamics model

The air taxi considered in this study has a novel configuration with several tilting EDFs distributed over the front and wing sections (see Fig. 2). High-fidelity modeling of aerodynamics is quite complicated for this configuration, considering that tilting EDFs also generate aerodynamic forces/moments through the ducted fan surfaces. Computational fluid dynamics (CFD) studies could estimate the aerodynamic forces and moments accurately. However, extensive work (time and cost) is required considering the wide flight envelope. A preliminary aerodynamic model containing the main aerodynamic effects at vertical and forward flight is generated. Some of the dominant effects are not modeled such as aero-propulsion couplings during the transition, ground effect at hover, etc. due to the complexity. The aerodynamic model is generated for hover and forward-flight model separately, and models are blended to obtain the transition dynamics.

The forward-flight model considers the effects of combined wing-body, and aerodynamic coefficients are estimated using open-source software called digital DATCOM [16]. Preliminary aerodynamic modeling at hover is more simple than the forward flight. The main aerodynamic effect is considered as the

https://doi.org/10.1017/aer.2023.87 Published online by Cambridge University Press

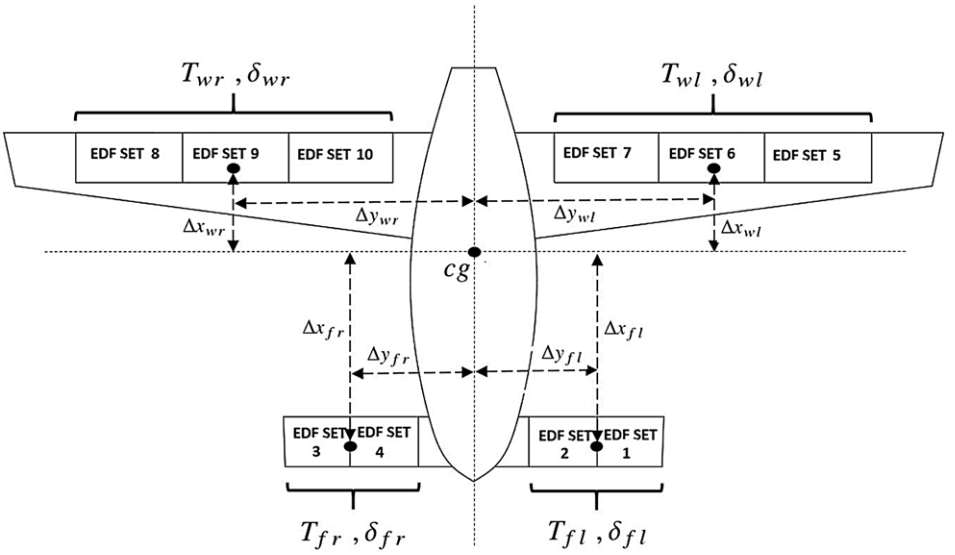


***Figure 2.*** *Top view and distribution of tilting EDFs on the wing and front sections.*

resistance force. A flat plate model is used to estimate the aerodynamic resistance force in all translational axes. A blending between the hover and forward aerodynamic model is applied to simulate the transition region. The blending considers that the wing-body aerodynamics is more dominant after 10 m/s airspeed. Due to the blending between hover and forward-flight models, simulation model has severe nonlinearities/couplings especially during the transition although some of the dominant effects (e.g. aero-propulsion couplings, ground effect) are not included into the preliminary flight dynamics modeling.

The modeling of the propulsion units is also kept straightforward. Datasheet of a commercially available small size EDF is used to estimate thrust and torque coefficients [17]. The effects of the mass flow rate for different airspeed and density conditions are not included in the model due to limited data. Similar to the aerodynamic modeling, extensive CFD studies are required for high-fidelity propulsion system modeling, which is not the main focus of this study. It is seen that a quadratic relation between rpm and thrust fits well to the EDF datasheet.

In the following sections, details of the aerodynamic modeling for hover, forward and transition flight phases are given first. Second, the EDF datasheet used to generate propulsion modeling is introduced. Finally, 6-DOF equations of motion (EOM) are defined at the end of the section.

### *2.1 Forward flight aerodynamic model: wing-body aerodynamics at high speeds*

The USAF Digital DATCOM is a computer program that estimates aerodynamic coefficients using semi-empiric methods [16, 18]. DATCOM has been used in literature and industry for a long time to build preliminary flight dynamics models of several aircraft and missiles [19–23]. It gives very fast and accurate enough results for the initial design phase [18–20]. Detailed verification of DATCOM methods are also studied in the literature [21, 24, 25]. To conclude, Digital DATCOM program is considered as an effective way to estimate the wing-body aerodynamics with acceptable accuracy since the main focus of the study is not detailed aerodynamic modeling. At this point, it is good to emphasise that detailed aerodynamic modeling of this unique aircraft is still an open area for researchers.

The input file of DATCOM for our case mainly contains 3-D geometry and desired flight conditions. The wing-body geometry of the aircraft is constructed iteratively to satisfy the following stability requirements [26] and aerodynamic efficiency at cruise represented as the lift-to-drag ratio ($C_L/C_D$).

https://doi.org/10.1017/aer.2023.87 Published online by Cambridge University Press

$$C_D = 0.1425 - 0.3395 \cdot M + 0.00038 \cdot (\alpha \cdot 180/pi)^2 + 0.5479 \cdot M^2$$

$$C_{yp} = -6.5 \cdot 10^{-5} \cdot \alpha \cdot 180/pi$$

$$C_{y\beta} = -0.0075$$

$$C_{Lq} = 0.3726$$

$$C_L = 0.1128 \cdot \alpha \cdot 180/pi$$

$$C_{lp} = -0.0093 - 7.37 \cdot 10^{-6} \cdot (\alpha \cdot 180/pi)^2$$

$$C_{l\beta} = -6.68 \cdot 10^{-5} \cdot \alpha \cdot 180/pi$$

$$C_{lr} = 4.21 \cdot 10^{-4} \cdot \alpha \cdot 180/pi$$

$$C_m = -0.0425 \cdot \alpha \cdot 180/pi$$

$$C_{mq} = -2.554$$

$$C_{n\beta} = -0.0066$$

$$C_{np} = -1.88 \cdot 10^{-4} \cdot \alpha \cdot 180/pi$$

$$C_{nr} = -1.11 \cdot 10^{-4} - 9.19 \cdot 10^{-6} \cdot (\alpha \cdot 180/pi)^2$$

***Figure 3.*** *Non-dimensional coefficients of the forward flight aerodynamic model obtained via Digital DATCOM.*

1. $C_{m\alpha} < 0 \equiv$ longitudinal static stability
2. $C_{n\beta} > 0 \equiv$ static directional(weathercock) stability (could not be satisfied due to the tailless design)
3. $C_{l\beta} < 0 \equiv$ lateral static stability
4. $C_{Y\beta} < 0 \equiv$ sideslip stability
5. $C_L/C_D > 5$ for $0 < \alpha_{cruise} < 10deg$, $\alpha_{cruise}$ is the angle-of-attack at cruise

Directional stability at forward flight could not be satisfied ($C_{n\beta}$ is negative, see Fig. 3). This is an expected result since the aircraft has no vertical tail [26]. As mentioned previously, not having conventional control and stability surfaces comes with several advantages. On the other hand, there are some drawbacks regarding the flight control such as open loop unstability in the directional channel, limited control authority and problems introduced by the couplings due to pure thrust vector control (i.e. couplings between control axis and control effectors).

Flight conditions are chosen according to the expected operation of the air taxi (see Table 1). Maximum airspeed is considered as 0.3 Mach ($\approx$ 100 m/s). Operations are assumed to be performed at low altitudes (0–1,000 m). It is observed that aerodynamic coefficients don't change significantly with respect to altitude for the considered altitude range. Therefore, sea level altitude is used in the DATCOM input file for simplicity. Digital DATCOM gives results at discrete flight conditions, which are represented as functions via curve-fitting (Fig. 3). The forward-flight model is dominant after 20 m/s airspeed. Therefore, the validity ranges of the functions are $-15\text{deg} < \alpha < +15deg$, $-15deg < \beta < +15$, $0.05 < \text{M} < 0.5$. Details of the DATCOM modeling, input file and non-dimensional coefficients (output of DATCOM) can be found in [27].

Overall static and dynamic contributions of the coefficients are given in Equation (1).

$$\left.\begin{aligned} C_{D,sta} &= C_D \\ C_{y,sta} &= C_{y\beta} \cdot \beta \cdot 180/\pi \\ C_{L,sta} &= C_L \\ C_{l,sta} &= C_{l\beta} \cdot \beta \cdot 180/\pi \\ C_{m,sta} &= C_m \\ C_{n,sta} &= C_{n\beta} \cdot \beta \cdot 180/\pi \end{aligned}\right\} \quad \left.\begin{aligned} C_{D,dyn} &= 0 \\ C_{y,dyn} &= C_{yp} \cdot p \cdot 180/\pi \cdot (b_{ref}/(2V_\infty)) \\ C_{L,dyn} &= (C_{Lq} \cdot q + C_{L\dot{\alpha}} \cdot \dot{\alpha}) \cdot 180/\pi \cdot (\bar{c}/(2V_\infty)) \\ C_{l,dyn} &= (C_{lp} \cdot p + C_{lr} \cdot r) \cdot 180/\pi \cdot (b_{ref}/(2V_\infty)) \\ C_{m,dy} &= (C_{mq} \cdot q + C_{m\dot{\alpha}} \cdot \dot{\alpha}) \cdot 180/\pi \cdot (\bar{c}/(2V_\infty)) \\ C_{n,dyn} &= (C_{np} \cdot p + C_{nr} \cdot r) \cdot 180/\pi \cdot (b_{ref}/(2V_\infty)) \end{aligned}\right\} \tag{1}$$

https://doi.org/10.1017/aer.2023.87 Published online by Cambridge University Press

***Table 1.*** *General parameters of the air taxi*

| Parameter | Symbol | Value | Unit |
|---|---|---|---|
| Maximum takeoff mass | $m$ | 500 | kg |
| Inertia matrix | $J = diag(I_x, I_y, I_z)$ | diag(353,732,1017) | $kgm^2$ |
| Wing span | $b_{ref}$ | 6.6 | m |
| Mean aerodynamic chord | $\bar{c}$ | 0.45 | m |
| Wing reference area | $S$ | 2.7 | $m^2$ |
| Fuselage length | $l_{fus}$ | 4 | m |
| Fuselage mean height | $h_{fus}$ | 2 | m |
| EDF thrust coefficient | $C_T$ | 1.2032e-04 | $Ns^2$ |
| EDF torque coefficient | $C_Q$ | 0.04 | m |
| Total number of EDF | – | 26 | – |
| Thrust to maximum takeoff weight ratio | $T/W_{MTOW}$ | 1.59 | – |
| Operation altitude | – | 0-1,000 | m |
| Cruise speed | – | $\approx 80$ | m/s |
| Maximum speed | – | $\approx 100$ | m/s |

Subscripts *sta* and *dyn* represent the static and dynamic contributions. $C_D, C_y, C_L$ are the non-dimensional drag, side-force and lift coefficients; $C_l, C_m, C_n$ are the non-dimensional moment coefficients in 3-axis; $V_\infty$ is the freestream velocity; $\alpha$ and $\beta$ represent the angle-of-attack and sideslip angle; $p, q, r$ are the body rotational rates; and $b_{ref}$ and $\bar{c}$ are the reference lengths defined in Table 1.

Equation (2) gives the overall forward-flight aerodynamic force and moment expressed in the body frame. It is noted that the DATCOM gives the coefficients in wind axes; however, the transformation from wind axes to body axes is considered insignificant due to the small angle-of-attack and sideslip angles.

$$F^b_{aero,forward} = \begin{bmatrix} -\bar{q}\,S C_{D,sta} \\ \bar{q}\,S(C_{y,sta} + C_{y,dyn}) \\ -\bar{q}\,S(C_{L,sta} + C_{L,dyn}) \end{bmatrix} \quad M^b_{aero,forward} = \begin{bmatrix} \bar{q}\,S(C_{l,sta} + C_{l,dyn})b_{ref} \\ \bar{q}\,S(C_{m,sta} + C_{m,dyn})\,\bar{c} \\ \bar{q}\,S(C_{n,sta} + C_{n,dyn})b_{ref} \end{bmatrix} \tag{2}$$

$\bar{q} = 1/2\rho V_\infty^2$ is the dynamic pressure with $\rho$ being the air-density. $S$ is the reference area defined in Table 1.

### *2.2 Hover flight aerodynamic model: resistance force at low speeds around hover*

During the low-speed flight around hover, the most dominant aerodynamic effect is the resistance drag force since aerodynamic lift and moments are negligible [28]. Ground effect is also relevant but it is not modeled for the scope of this study. The low-speed flight around hover is restricted to 10 m/s for horizontal flight and 5 m/s for vertical flight.

In a study about modeling and flight control of a fixed wing VTOL aircraft, the preliminary hover model is based on flat plate aerodynamic modeling [28]. A similar approach is used to generate a preliminary aerodynamic model at hover. Drag resistance is roughly estimated for each direction based on a rectangular flat-plate model for the y and z directions, and a circular cylinder model for the x-direction. The frontal areas used in the estimations are calculated as follows. $l_{fus}$, $h_{fus}$, and $S$ are defined in Table 1.

$$S_x = \pi h_{fus}^2/4 \approx 3m^2, \quad S_y = l_{fus}h_{fus} = 8m^2, \quad S_z = l_{fus}h_{fus} + S \approx 10m^2 \tag{3}$$

https://doi.org/10.1017/aer.2023.87 Published online by Cambridge University Press

***Table 2.*** *Parameters of the Schubeler DS-215-DIA HST EDF*

| Parameter | Value |
|---|---|
| Mass | 3.4 kg |
| Diameter | 21 cm |
| Maximum thrust | 250 N |
| Maximum torque | 10 Nm |
| Maximum power | 15.6 kW |
| Overall efficiency | 78% |

Based on the frontal areas, aerodynamic drag resistance force around hover is expressed in body coordinates as in Equation (4). Aircraft can move forward/backward and sideward around the hover so that the sign function is added to include the direction of motion into the equations. Body velocities ($u$, $v$, $w$) are used in the equations assuming that roll and pitch angles are small for the low-speed flight around hover. The drag coefficients for the y and z directions ($C_{d,y}$ and $C_{d,z}$) are equal to 1.2 for a rectangular plate, and the drag coefficient for the x-direction ($C_{d,x}$) is equal to 0.74 for a circular cylinder [29].

$$F^b_{aero,hover} = \begin{bmatrix} -sign\,(u)\,0.5\rho u^2 S_x C_{d,x} \\ -sign\,(v)\,0.5\rho v^2 S_y C_{d,y} \\ -sign\,(w)\,0.5\rho w^2 S_z C_{d,z} \end{bmatrix} \tag{4}$$

### *2.3 Complete aerodynamic model*

For high- and low-speed regions, aerodynamic models are generated separately in previous sections. These models are merged to express the complete aerodynamic model considering the transition. The merging/decision parameter is chosen as body x velocity ($u$). The airspeed ($V_{\text{inf}}$) is not used as a decision parameter since it increases during the sideward motion, but the wing does not generate lift.

Based on the DATCOM results, the wing-body aerodynamics seems to be dominant after 20 m/s (0.05 Mach) so that the forward flight model is fully active after $u = 20\text{m/s}$. Transition from hover to forward aerodynamic model starts at $u = 10\text{m/s}$.

The complete aerodynamic model is given as a combination of the hover and forward aerodynamic models in Equation (5) via introducing the merging coefficient $k_{aero}$.

$$\left.\begin{aligned} F^b_{aero} &= (1-k_{aero})F^b_{aero,forward} + k_{aero}F^b_{aero,hover} \\ M^b_{aero} &= (1-k_{aero})M^b_{aero,forward} \end{aligned}\right\} \quad k_{aero} = \begin{cases} 1 & \text{u} < 10 \\ (20-u)/10 & 10 \le \text{u} \le 20 \\ 0 & \text{u} > 20 \end{cases} \tag{5}$$

### *2.4 Propulsion system modelling*

The propulsion system consists of several EDFs distributed over the wing and front sections (Fig. 2). The datasheet of a commercially available EDF named Schubeler DS-215-DIA HST is used [17] to estimate the thrust and torque generated by each EDF. A similar EDF is also used in a NASA founded DEP aircraft project [30]. The basic parameters of the EDF are given in Table 2.

Based on the datasheet, thrust ($T$) and torque ($Q$) of each EDF are modeled as follows. Values of $C_T$ and $C_Q$ are defined in Table 1.

$$T = C_T(rpm2\pi/60)^2, \quad Q = C_Q T \tag{6}$$

Derivation of the total force and moment generated by the propulsion systems depends on the distribution of EDFs over the wing and front sections (Fig. 2) and the thrust vector control concept (Fig. 4). Tilt angle ($\delta$) and thrust ($T$) of EDFs are adjusted to control the air taxi. Since rpm is related to thrust with

https://doi.org/10.1017/aer.2023.87 Published online by Cambridge University Press

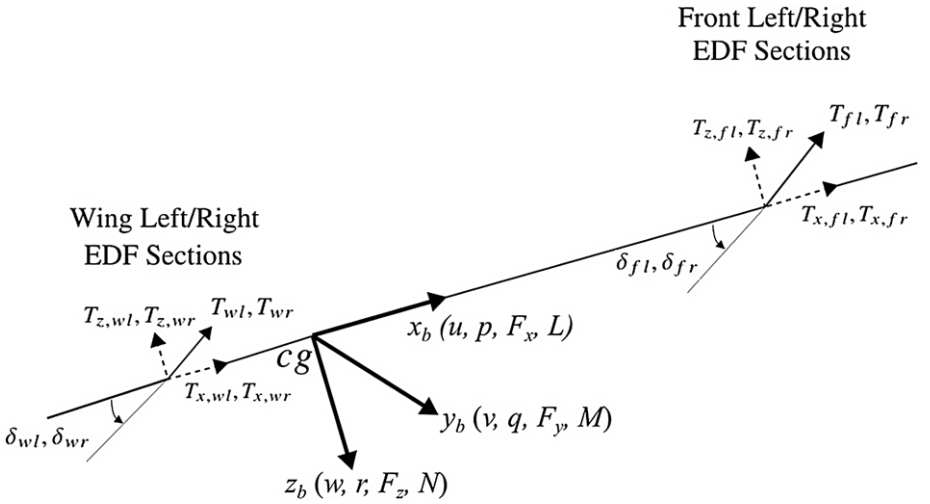


***Figure 4.*** *Thrust vector control concept, side view.*

a constant coefficient (i.e. $C_T$), thrust is used as a control parameter instead of rpm for simplicity. There are 26 EDFs with 18 distributed over the wings and 8 on the front. Distribution of 26 EDFs between the front and wing sections is based on the pitch moment balance at hover (see EDF lever arms info in Table 3, and top view in Fig. 2). There are six EDF sets (each has three EDF) on the wings and four EDF sets (each has two EDF) on the front sections (Fig. 2). EDF sets are combined for left/right front and wing sections to simplify the controller design. By this way number of control inputs is reduced to eight (i.e. four tilt angle ($\delta_{wl}$, $\delta_{wr}$, $\delta_{fl}$, $\delta_{fr}$) and four thrust ($T_{wl}$, $T_{wr}$, $T_{fl}$, $T_{fr}$) for each EDF section). It is also noted that the average lever arms defined in Table 3 are used in the controller. Lever arm information is a direct input to the controller so that it is possible to manipulate this input properly in case of failures or any other required corrections. Table 3 gives the detailed EDF parameters for the left/right wing and front sections.

Based on the thrust vector concept illustrated in Fig. 4, total force and moment generated at each section (front left, front right, wing left and, wing right) in the body coordinate system are represented in a general equation form as follows. The parameters used in the following equations are given in Table 3.

$$F_i^b = \begin{bmatrix} \cos(\delta_i) & 0 & \sin(\delta_i) \\ 0 & 1 & 0 \\ -\sin(\delta_i) & 0 & \cos(\delta_i) \end{bmatrix} \begin{bmatrix} \mathrm{T_i} \\ 0 \\ 0 \end{bmatrix} n_i = \begin{bmatrix} \cos(\delta_i)\,\mathrm{T_i} \\ 0 \\ -\sin(\delta_i)\,\mathrm{T_i} \end{bmatrix} n_i, \quad with \quad i = fl, fr, wl, wr \tag{7}$$

$$M_i^b = \begin{bmatrix} \cos(\delta_i) & 0 & \sin(\delta_i) \\ 0 & 1 & 0 \\ -\sin(\delta_i) & 0 & \cos(\delta_i) \end{bmatrix} \begin{bmatrix} \mathrm{Q_i} \\ 0 \\ 0 \end{bmatrix} td_i n_i + \begin{bmatrix} \Delta \mathrm{x_i} \\ \Delta \mathrm{y_i} \\ \Delta \mathrm{z_i} \end{bmatrix} \times \begin{bmatrix} \cos(\delta_i)\,\mathrm{T_i} \\ 0 \\ -\sin(\delta_i)\,\mathrm{T_i} \end{bmatrix} n_i, \quad with \quad i = fl, fr, wl, wr \tag{8}$$

Then, the overall propulsion force and moment in the body coordinate system ($F^b_{prop}$ and $M^b_{prop}$) are the sum of each section.

$$\left.\begin{aligned} F^b_{prop} &= [Fx_{prop} \quad 0 \quad Fz_{prop}]^T = F^b_{fl} + F^b_{fr} + F^b_{wl} + F^b_{wr} \\ M^b_{prop} &= [L_{prop} \quad M_{prop} \quad N_{prop}]^T = M^b_{fl} + M^b_{fr} + M^b_{wl} + M^b_{wr} \end{aligned}\right\} \tag{9}$$

https://doi.org/10.1017/aer.2023.87 Published online by Cambridge University Press

***Table 3.*** *Parameters of the EDF sections*

| Section name & Subscript | Number EDFs $n$ | Turn direction $td$ | Mean x-lever arm $\Delta x$ | Mean y-lever arm $\Delta y$ | Tilt angle $\delta$ | Thrust $T$ |
|---|---|---|---|---|---|---|
| Front left, $()_{fl}$ | 9 | CCW(+1) | 2.1 m | −0.8 m | $\delta_{fl}$ | $T_{fl}$ |
| Front right, $()_{fr}$ | 9 | CW(–1) | 2.1 m | 0.8 m | $\delta_{fr}$ | $T_{fr}$ |
| Wing left, $()_{wl}$ | 4 | CW(–1) | −0.85 m | −2.05 m | $\delta_{wl}$ | $T_{wl}$ |
| Wing right, $()_{wr}$ | 4 | CCW(+1) | −0.85 m | 2.05 m | $\delta_{wr}$ | $T_{wr}$ |

***Table 4.*** *Parameters of actuator dynamics*

| Control input | Natural freq. | Damping ratio | Minimum | Maximum | Rate limit |
|---|---|---|---|---|---|
| $T_{fl}$ & $T_{fr}$ | 25 rad/s | 1 | 0 N | 1,200 N | – |
| $T_{wl}$ & $T_{wr}$ | 25 rad/s | 1 | 0 N | 2,700 N | – |
| $\delta_{fl}$ & $\delta_{fr}$ | 10 rad/s | 1 | −30 deg | 120 deg | ± 90 deg/s |
| $\delta_{wl}$ & $\delta_{wr}$ | 10 rad/s | 1 | 0 deg | 120 deg | ± 90 deg/s |

### *2.5 Actuator dynamics*

There are two control inputs for each EDF, which are the thrust ($T$) and the tilt angle ($\delta$). Thrust dynamics of a similar Schubeler EDF considered in this study is modeled in a work based on the wind-tunnel data as a second order system with a natural frequency of 18.85 rad/s and damping ratio of 1 [31]. Moreover, the maximum thrust of a Schubeler EDF is given as 250 N in the datasheet (Table 2). Based on these reference values, a little improved EDF system with a maximum thrust of 300 N ($\approx$ 15,000 rpm) and a natural frequency of 25 rad/s is used in this study. The overall parameters of the thrust dynamics are given in Table 4, considering the number of EDFs in the front and wing sections (Table 3).

There is no data to be used for the tilting dynamics of EDFs. Considering the small size/mass of Schuler EDF (Table 2), the required hinge-moments to rotate the EDF sets are relatively small. For this reason, it is reasonable to assume quite fast tilting dynamics. Regarding the tilt angle limits, the wing EDF sets are constrained to 0° tilt angle, which is a limitation applied due to the wing structure. For EDFs at the front section there is no fixed structure, so that the minimum tilt angle is constrained to −30°. For both the front and wing EDFs, the maximum tilt angle is chosen as 120°. The overall parameters of the tilt angle actuator dynamics are also given in Table 4.

### *2.6 Six DOF equations of motion*

Six degree of freedom (6-DOF) equations of motion are obtained by using the overall aerodynamic and propulsion forces/moments defined in Equations (5) and (9), respectively.

$$\begin{bmatrix} \dot{u} \\ \dot{v} \\ \dot{w} \end{bmatrix} = (F^b_{aero} + F^b_{prop} + F^b_{grav} + F^b_{dist})/m - \begin{bmatrix} p \\ q \\ r \end{bmatrix} \times \begin{bmatrix} u \\ v \\ w \end{bmatrix}, \quad with \quad F^b_{grav} = \begin{bmatrix} -g\sin(\theta) \\ g\sin(\phi)\cos(\theta) \\ g\cos(\phi)\cos(\theta) \end{bmatrix} \tag{10}$$

$$\begin{bmatrix} \dot{p} \\ \dot{q} \\ \dot{r} \end{bmatrix} = J^{-1} \left( M^b_{aero} + M^b_{prop} + M^b_{dist} - \begin{bmatrix} p \\ q \\ r \end{bmatrix} \times J \begin{bmatrix} p \\ q \\ r \end{bmatrix} \right) \tag{11}$$

$F^b_{grav}$ represents the gravitational force in the body coordinates, with $\phi$ and $\theta$ being the roll and pitch angles. $m$ and $J$ are the mass and inertia matrix defined in Table 1. $F^b_{dist}$ and $M^b_{dist}$ are the disturbance

https://doi.org/10.1017/aer.2023.87 Published online by Cambridge University Press

force and moment introduced in the simulations to test the disturbance rejection characteristics of the designed controller.

## 3.0 Nonlinear flight controller design

The aim is to design an unified flight controller for the novel air taxi considering the wide flight envelope that includes: vertical takeoff and climb, hover, transition to forward flight, cruise, climb/descent and turns, transition to hover and vertical landing. After a certain airspeed, the wing-body aerodynamics becomes more dominant such that significant nonlinearities occur during the transition manoeuvers. Additional nonlinearities are experienced, especially during the transition, due to the thrust vector control's coupled nature. Considering these nonlinearities, it is beneficial to use a nonlinear control method to design the unified flight controller. INDI approach fits well to the flight control problems of this unique concept.

INDI is introduced in the late 1990s as an incremental form of the nonlinear dynamic inversion (NDI) [32, 33]. NDI, also called feedback linearisation, is a model-based approach that emerges as an alternative to the classical gain-scheduling controller design [34]. NDI has become very popular since it can handle all of the modeled nonlinearities using a generic and straightforward formulation. On the other hand, it is highly sensitive to modeling errors and disturbances [35]. For unique aircraft concepts such as the one considered in this study, extensive modeling effort is needed to have an accurate flight dynamics model to be used in the NDI. INDI's main difference is relying on the sensor data (measurement and/or estimation) instead of the aircraft model to perform the dynamic inversion [36]. In this way, sensitivity to the modeling errors (including the failures) and disturbances reduce significantly [35]. This advantage is crucial considering the quite complex flight dynamic models of unique aircraft concepts.

On the other hand, INDI is highly sensitive to the sensor data, which is mostly used as translational and rotational acceleration feedback in the control loop. Due to this sensitivity, the INDI controller's performance is highly related to accurate estimation of the acceleration feedback with low noise level and small time delays [35]. The first studies about INDI focus more on the improved robustness to modeling errors compared to the conventional nonlinear dynamic inversion [32, 33, 37]. In the following years, there have been studies that concern the INDI's robustness properties to the acceleration feedback [36, 38]. Moreover, availability and/or estimation of the acceleration feedback with less noise and delay are also studied [35]. Regarding the practical side, real-time implementation of INDI becomes very important since the sensor-dependent nature of INDI makes it questionable for the practical applications. A study conducted by the German Aerospace Center (DLR) focuses on real-time implementation of INDI-based flight controller for a large scale Cessna-type aircraft [39]. Another research applied at Delft University analyses the INDI's disturbance rejection properties via indoor flight tests on micro air vehicles (MAVs) [40]. These successful real-time implementations are very valuable to show the potentials and possible improvements of the INDI-based flight controller.

The air taxi concept studied in this work has no conventional control surfaces, and flight control is achieved by adequately adjusting the thrust vector (rpm and tilt angle) of several EDFs. For aircraft with conventional control surfaces, it is possible to decouple aileron, elevator and rudder to generate desired moments in three-axis via a unique solution [41, 42]. Also, resolving the problems due to the actuator saturation is more straightforward thanks to the decoupled nature of the control axis/channels and control effectors/actuators [42]. However, for our case, it is harder to relate the actuator limitations with the control axis due to the highly coupled nature of the thrust vector control and also the over-actuation [43]. If a large and permanent discrepancy/error between the commanded and physically achieved moment commands occur due to the limited control authority, then stable flight can not be achieved. CA methods can be used to make sure that the limited control authority is appropriately allocated to guarantee the stable flight for the entire flight [43]. Several CA methods are studied in the literature, and two survey papers give a detailed description and advantages/disadvantages of these approaches considering specific applications [42, 44]. The basic CA methods, such as explicit ganging, redistributed pseudo inverse, or daisy

https://doi.org/10.1017/aer.2023.87 Published online by Cambridge University Press

chaining are easy to implement. However, they may not give an acceptable performance in case of actuator limitations [43]. More complex methods are based on constrained optimisation problems, which are more effective especially considering the actuator limitations [42, 43]. The problem of constrained optimisation is the required computer time and power in real time applications [42]. However, with the increasing capabilities of computer technology, optimisation-based control allocation approaches gained more popularity [42, 44]. In this study, an efficient active set algorithm [45] is adapted to solve the CA problem defined as a constrained optimisation problem. The CA is integrated into the INDI structure to handle the absolute actuator limitations effectively. Details of the CA design is given in Section 3.3. It is observed that the CA has a crucial role in prioritising the stability-related channels in case of the limited control authority. Simulation results show that the stable flight could not be achieved for specific cases without the proper control allocation.

In this section, control inputs are defined in general first. Then, the formulation of the INDI controller is given in detail. Finally, the CA design and integration into the INDI controller are explained.

### *3.1 Control input definitions*

Before diving into the formulation of the INDI control law, control inputs are defined first. As shown in Fig. 4, the thrust vector is adjusted to control both translational and rotational dynamics. Tilt angle and rpm are the physical actuator states, but for simplification, thrust is used instead of rpm based on the relation given in Equation (6). Using this simplification, the control input vector on the physical actuator level includes the tilt angles($\delta$) and thrust magnitudes($T$). $U_{act}$ and $U$ represent the physical level control inputs with and without considering the actuator dynamics, respectively. $U_{act}$ and $U$ are separately defined to check the CA performance (see Section 4 for details). On the aircraft level, our aim is to generate desired forces and moments via controlling the thrust vector. Therefore, a virtual control input vector ($v_{INDI}$) that includes the forces and moments generated by the propulsion system on body axes, defined in Equation (9), is introduced. Moreover, to get rid of the nonlinearities of the thrust vector concept, the INDI control input vector ($U_{INDI}$) is defined considering the thrust contribution on the body x and z directions (Fig. 4). In this way, it is possible to relate the virtual and INDI control inputs using only the lever arm information, data input to the controller, and calculated using simple geometry. Equation (12) gives the definitions and relations of the different control inputs. The naming convention of the control inputs and other data such as the mean lever arms are given in Table 3.

$$
\begin{aligned}
&U = \begin{bmatrix} T_{fl} & T_{fr} & T_{wl} & T_{wr} & \delta_{fl} & \delta_{fr} & \delta_{wl} & \delta_{wr} \end{bmatrix}^T \\
&U_{act} = \begin{bmatrix} T_{fl,act} & T_{fr,act} & T_{wl,act} & T_{wr,act} & \delta_{fl,act} & \delta_{fr,act} & \delta_{wl,act} & \delta_{wr,act} \end{bmatrix}^T \\
&T_x = sin(\pi/2 - \delta)T, \quad T_z = cos(\pi/2 - \delta)T, \quad T = \sqrt{T_x^2 + T_z^2} \\
&v_{INDI} = \begin{bmatrix} L_{prop} & M_{prop} & N_{prop} & Fz_{prop} & Fx_{prop} \end{bmatrix}^T \\
&U_{INDI} = \begin{bmatrix} T_{x,fl} & T_{x,fr} & T_{x,wl} & T_{x,wr} & T_{z,fl} & T_{z,fr} & T_{z,wl} & T_{z,wr} \end{bmatrix}^T \\
&v_{INDI} = T_{v,INDI} U_{INDI}, \quad U_{INDI} = T_{v,INDI}^{-1} v_{INDI}, \quad T_{v,INDI}^{-1} = T_{v,INDI}^T (T_{v,INDI} T_{v,INDI}^T)^{-1}
\end{aligned}
$$

$$
\begin{bmatrix} L_{prop} \\ M_{prop} \\ N_{prop} \\ Fz_{prop} \\ Fx_{prop} \end{bmatrix} = \begin{bmatrix} 0 & 0 & 0 & 0 & \Delta y_{fl} & -\Delta y_{fr} & \Delta y_{wl} & -\Delta y_{wr} \\ 0 & 0 & 0 & 0 & \Delta x_{fl} & \Delta x_{fr} & -\Delta x_{wl} & -\Delta x_{wr} \\ \Delta y_{fl} & -\Delta y_{fr} & \Delta y_{wl} & -\Delta y_{wr} & 0 & 0 & 0 & 0 \\ 0 & 0 & 0 & 0 & -1 & -1 & -1 & -1 \\ 1 & 1 & 1 & 1 & 0 & 0 & 0 & 0 \end{bmatrix} \begin{bmatrix} T_{x,fl} \\ T_{x,fr} \\ T_{x,wl} \\ T_{x,wr} \\ T_{z,fl} \\ T_{z,fr} \\ T_{z,wl} \\ T_{z,wr} \end{bmatrix} \tag{12}
$$

https://doi.org/10.1017/aer.2023.87 Published online by Cambridge University Press

As formulated in Equation (12), system is over-actuated since there are eight control effectors to control five axis/channels ($L, M, N, Fz, Fx$ and noted that side-force $Fy$ is indirectly controlled via roll angle ($\phi$)-roll moment($L$), see Section 3.2.1 for details). Pseudo-inverse approach is used to find solution for the over-actuated system. However, pseudo-inverse approach is not sufficient to find a solution that allocates the limited control authority properly to guarantee stable flight in case of actuator saturation. Therefore, additional consideration is needed regarding the CA design to take into account actuator saturation. Details of the CA design and its criticality are discussed in Section 3.3.

### *3.2 Formulation of the INDI control law*

State space representation of the EOM defined in Equations (10) and (11) can be rewritten in a control-affine form.

$$\dot{x} = f(x) + g \quad v_{INDI}, \quad x = \begin{bmatrix} \mathrm{p} & \mathrm{q} & \mathrm{r} & \mathrm{w} & \mathrm{u} \end{bmatrix}^T, \quad g = diag\left(1/I_x, \quad 1/I_y, \quad 1/I_z, \quad 1/m, \quad 1/m\right) \tag{13}$$

In Equation (13), $f(x)$ includes all the components other than the propulsion forces and moments that are defined as the virtual control input ($v_{INDI}$) in Equation (12). State vector ($x$) does not contain the body y-velocity ($v$) since the propulsion system can not directly generate forces on the body y-direction. As explained later, the roll and yaw angle outer loop controllers are used to indirectly control the motion on body y-direction for low and high speed flight.

Once the control-affine state space representation is defined, it is possible to write the first-order Taylor series approximation evaluated at the previous time step (subscript "0") of the states and the virtual control input.

$$\dot{x} \approx \dot{x}_0 + \left.\frac{\partial\left[f(x)+gv_{INDI}\right]}{\partial x}\right|_{\substack{x=x_0 \\ v_{INDI}=v_{INDI,0}}} (x - x_0) + \left.\frac{\partial\left[f(x)+gv_{INDI}\right]}{\partial v_{INDI}}\right|_{\substack{x=x_0 \\ v_{INDI}=v_{INDI,0}}} (v_{INDI} - v_{INDI,0}) \tag{14}$$

The primary assumption of the INDI approach is the time-scale separation principle. Suppose the actuator dynamics are relatively fast, and the time step is small enough. In that case, it is possible to assume that the changes in states are relatively small compared to the changes in control inputs during a single time step [35, 39]. Considering the fast thrust/rpm dynamics of EDFs and 100 Hz sample time, time scale separation fits well with the problem. Regarding the tilting dynamics of EDFs (see Table 4), it is much slower than the thrust/rpm dynamics, so that time scale separation principle may not be satisfied. This was one of the open questions at the beginning of the study. However, simulation results show that the proposed tilt angle dynamics is also fast enough to satisfy the time scale separation principle. Then, state term is assumed negligible and removed from the Taylor series expansion based on the time-scale separation principle.

$$\dot{x} \approx \dot{x}_0 + g(v_{INDI} - v_{INDI,0}) = \dot{x}_0 + g\Delta v_{INDI} \tag{15}$$

Inverting Equation (15) and also using the relations given in Equation (12), the incremental form of the virtual and INDI control inputs ($\Delta v_{INDI}$ and $\Delta U_{INDI}$) are found.

$$\begin{aligned} &\Delta v_{INDI} = g^{-1}(\dot{x} - \dot{x}_0), \ \ where \ \dot{x} = \dot{x}_{req} \\ &\Delta U_{INDI} = T_{v,INDI}^{-1} \Delta v_{INDI} \end{aligned} \tag{16}$$

The incremental INDI control input depends on the following terms:

- $\dot{x}_0$: The state derivative vector evaluated using the current and previous values of sensor outputs. A simple 2nd order filter is used to filter the noise due to the derivative. See Section 3.2.2.
- $\dot{x}_{req}$: The required state derivative vector to track the attitude and velocity commands. A simple linear controller based on kinematic relations is defined in Section 3.2.1 to generate $\dot{x}_{req}$.
- $g^{-1}$: The inverse of $g$ matrix, which depends only on the inertia and mass. See Equation (13).

https://doi.org/10.1017/aer.2023.87 Published online by Cambridge University Press

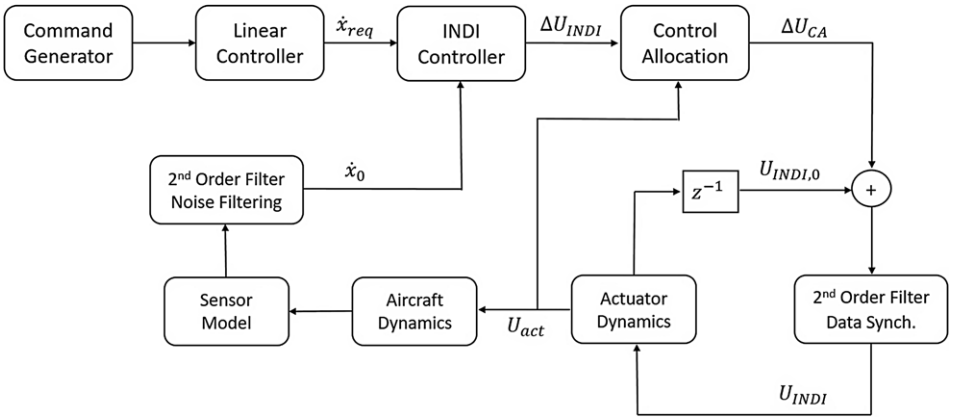


***Figure 5.*** *High-level block diagram of the simulation model.*

- $T_{v,INDI}^{-1}$: Pseudo inverse of $T_{v,INDI}$ matrix, which depends only on the mean lever arms. See Equation (12).

The mean lever arms are calculated based on the geometry (Fig. 2), and it is assumed that this information is an input to the controller similar to the mass and inertia. If actuator failures occur in some EDFs, then the mean lever arm change accordingly. To sum up, the incremental INDI control input only depends on the mass/inertia and the lever arms (geometry) of the aircraft. The flight dynamics model information required for the dynamic inversion is replaced with the state derivative estimation based on the sensor measurements. This is a significant advantage regarding the improved robustness, especially designing a controller for a novel aircraft that is hard to model accurately. However, INDI becomes sensitive to the noise and delay introduced by the state derivative estimation using the sensor measurements. Filtering is required to reduce the noise level and to improve the INDI performance. It is crucial to test the INDI controller with a realistic sensor model due to the sensitivity. More information will be given about the sensor model and noise filtering in Section 3.2.2.

The overall INDI control input is represented as following, again $U_{INDI,0}$ represents the control input at the previous time step. It is important to note that the filter applied to estimate the state derivatives is also applied to the INDI control input to satisfy the data synchronisation (see Fig. 5).

$$U_{INDI} = U_{INDI,0} + \Delta U_{INDI} \tag{17}$$

*3.2.1 Linear controller: obtaining the required state derivatives*

The aim is to control the aircraft's attitude and velocity, and it is possible to generate the required state derivatives using a proportional-derivative (PD) type linear controller as follows. The linear controller gains are defined in Table 5.

$$\left.\begin{aligned}
\dot{x}_{req} &= \begin{bmatrix} \dot{p}_{req} & \dot{q}_{req} & \dot{r}_{req} & \dot{w}_{req} & \dot{u}_{req} \end{bmatrix}^T \\
\dot{p}_{req} &= (\phi_{cmd} - \phi)K_{\phi} + (\dot{\phi}_{cmd} - \dot{\phi})K_{\dot{\phi}} \\
\dot{q}_{req} &= (\theta_{cmd} - \theta)K_{\theta} + (\dot{\theta}_{cmd} - \dot{\theta})K_{\dot{\theta}} \\
\dot{r}_{req} &= (\psi_{cmd} - \psi)K_{\psi} + (\dot{\psi}_{cmd} - \dot{\psi})K_{\dot{\psi}} \\
\dot{w}_{req} &= (w_{cmd} - w)K_{w} + (\dot{w}_{cmd} - \dot{w})K_{\dot{w}} \\
\dot{u}_{req} &= (u_{cmd} - u)K_{u} + (\dot{u}_{cmd} - \dot{u})K_{\dot{u}}
\end{aligned}\right\} \tag{18}$$

https://doi.org/10.1017/aer.2023.87 Published online by Cambridge University Press

***Table 5.*** *Gains of the linear controller*

| Attitude Loop gains | Value | Velocity Loop gains | Value | Outer Loop gains | Value |
|---|---|---|---|---|---|
| $K_\phi$ | 3 | $K_w$ | 1.5 | $K_h$ | 0.5 |
| $K_{\dot{\phi}}$ | 5 | $K_{\dot{w}}$ | 0.5 | $K_{\dot{h}}$ | 1 |
| $K_\theta$ | 3 | $K_u$ | 1.5 | $K_v$ | 5 |
| $K_{\dot{\theta}}$ | 5 | $K_{\dot{u}}$ | 0.5 | $K_{\dot{v}}$ | 3 |
| $K_\psi$ | 1.5 | | | | |
| $K_{\dot{\psi}}$ | 3 | | | | |

As mentioned before, the velocity in body y-direction ($v$) is not included in the equations since EDFs do not directly generate forces in this direction. To control the aircraft motion in body y-direction, an outer loop controller is used. Outer loop controller generates the required roll angle $\phi_{cmd,nav,hover}$ at low speeds to track the body y-velocity command ($v_{cmd}$). $\phi_{cmd,nav,hover}$ is limited to $\pm$ 30 deg to avoid large bank angles considering the safety and limited thrust authority. Similarly, to control the altitude ($h$) at low speeds, the vertical velocity command $w_{cmd,nav,hover}$ is generated by the outer loop altitude controller. To control the flight path angle ($\gamma$) at high speeds, commands of pitch angle ($\theta_{cmd,fpa}$) and body velocities, which corresponds to a specific angle-of-attack ($w_{cmd,fpa}, u_{cmd,fpa}$) and are applied simultaneously. It is also possible to control the angle-of-attack ($\alpha$) by using a similar approach. At high speeds, coordinated turns are performed via applying a yaw angle command ($\psi_{cmd,coord,turn}$) based on the coordinated turn equation defined in Ref. (46). Details of the command generation logic and the transition speeds are explained in Section 3.2.3.

A manual command (with the subscript *cmd*, *manual*) is also defined for each channel to have a direct pilot command, which is primarily added to test the controller's performance. To sum up, the attitude and velocity commands sent to the linear controller defined in Equation (18) are expressed as follows. $\phi_{cmd}, \theta_{cmd}, \psi_{cmd}$ represents the total roll, pitch and yaw angle commands; whereas, $w_{cmd}$ and $u_{cmd}$ are the total velocity commands in body z and x directions, respectively.

$$\left.\begin{aligned} \phi_{cmd} = \phi_{cmd,manual} + \phi_{cmd,nav,hover} \quad with \quad \phi_{cmd,nav,hover} &= (v_{cmd} - v)K_v + (\dot{v}_{cmd} - \dot{v})K_{\dot{v}} \\ \theta_{cmd} &= \theta_{cmd,manual} + \theta_{cmd,fpa} \\ \psi_{cmd} &= \psi_{cmd,manual} + \psi_{cmd,coord,turn} \\ w_{cmd} = w_{cmd,manual} + w_{cmd,nav,hover} + w_{cmd,fpa} \quad with \quad w_{cmd,nav,hover} &= (h_{cmd} - h)K_h + (\dot{h}_{cmd} - \dot{h})K_{\dot{h}} \\ u_{cmd} &= u_{cmd,manual} + u_{cmd,fpa} \end{aligned}\right\} \quad (19)$$

It is noted that the linear controller uses the kinematic relations and independent from the aircraft model. Therefore, tuning can be performed easily, and the gains of the linear controller are given in the following table.

*3.2.2 Sensor model & noise filtering*

It is mentioned that the INDI method highly depends on the sensor measurements. Therefore, using a realistic sensor model is essential to test the controller performance. As defined in Equation (16), the controller requires derivatives of the body rotational and translational velocities. The derivative of gyroscope measurements is used to obtain the rotational accelerations; whereas, the translational accelerations can be directly obtained via accelerometer sensors. Based on the noise data of a MEMS IMU sensor studied in Ref. (47), the noise level of gyroscope and accelerometer sensors are taken as 1deg/s and 0.1m/s$^2$, respectively. Time delay introduced by the sensor dynamics is taken as 10 ms based on a similar study that focuses on the effect of the sensor dynamics on an INDI based controller [36].

https://doi.org/10.1017/aer.2023.87 Published online by Cambridge University Press

A second order linear filter is applied to the sensor measurements to reduce the noise. The filter parameters taken from a study about INDI control [28] are a natural frequency of 80 rad/s and a damping ratio of 1. As mentioned previously, the same filter is also applied to the INDI control input to satisfy data synchronisation. More explanations about the noise filtering and data synchronisation are given in Ref. (27).

#### *3.2.3 Command generator*

Attitude and body velocity commands defined in Equation (19) are generated considering the flight envelope. At low speeds around hover, y-direction is controlled by $\phi_{cmd,nav,hover}$. This command's contribution to the total roll angle command ($\phi_{cmd}$) goes to zero smoothly with the increasing speed. Similarly, $w_{cmd,nav,hover}$ is generated to control the altitude at low speeds, and this command does not have a contribution to the total body z-velocity command ($w_{cmd}$) at high speeds. $\phi_{cmd,nav,hover}$ is effective until 20 m/s ground speed, whereas $w_{cmd,nav,hover}$ is effective until 50 m/s airspeed to keep the altitude until the fixed wings generate significant amount of aerodynamic lift. After 50 m/s, the flight path angle is controlled by applying combined commands explained in the next paragraph.

The transition from hover to forward flight is achieved by commanding body x-velocity ($u_{cmd}$) up to the cruise speed. It is possible to control the flight path angle at high speeds by commanding combined pitch angle and body velocities ($\theta_{cmd,fpa}$ and $w_{cmd,fpa}$, $u_{cmd,fpa}$). During cruise flight, it is also possible to achieve the desired angle-of-attack by applying a similar strategy. Applying combined pitch angle and body velocity commands are effective after 50 m/s airspeed. Coordinated turns are also possible after 20 m/s airspeed via generating the $\psi_{cmd,coord,turn}$.

All commands are generated using second-order transfer functions and saturation limits considering both the handling qualities and safe flight.

### *3.3 Control allocation design and integration into the INDI controller*

As mentioned in Section 3.1, the system is over-actuated and properly allocating the limited control authority in case of actuator saturation requires specific CA design. Based on the simulation results (Section 4.4), in the presence of severe disturbances (gusts/failures etc.), actuator saturation can cause stability problems if it is not handled properly. The INDI controller generates the incremental control input without considering the actuator limitations in the controller design. This could lead to large errors between the commanded and physically achieved forces and moments in case of severe actuator limitations. The CA becomes active in case of actuator limitations and allocates the limited control authority accordingly to guarantee stable flight.

If the INDI controller generates actuator commands beyond the minimum and maximum thrust and/or tilt angle, then the constrained optimisation problem given as follows is solved iteratively using the active set algorithm defined in Ref. (45).

$$\left.\begin{aligned} \Delta U_{CA} &= [\Delta_{T_{x,fl}} \Delta_{T_{x,fr}} \Delta_{T_{x,wl}} \Delta_{T_{x,wr}} \Delta_{T_{z,fl}} \Delta_{T_{z,fr}} \Delta_{T_{z,wl}} \Delta_{T_{z,wr}}]^T \\ \underset{\Delta U_{CA}}{\text{minimize}} \quad & J(\Delta U_{CA}) = \| W_u(\Delta U_{CA} - \Delta U_{des})\|^2 + \gamma \| W_v(T_{v,INDI}\Delta U_{CA} - \Delta v_{INDI})\|^2 \\ \text{subject to} \quad & \Delta U_{CA,min} < \Delta U_{CA} < \Delta U_{CA,max} \\ \text{with initial conditions} \quad & \Delta U_{INDI} \end{aligned}\right\} \tag{20}$$

The cost function is represented as a quadratic mixed optimisation problem with two parts named control minimisation and error minimisation [42]. CA focus on error minimisation by prioritising the moment channels over the force channels in case of limited control authority (i.e. actuator saturation). This is achieved by selecting the corresponding weight matrix as $W_v = diag(1000, 1000, 100, 50, 50)$. Note that the weights of $W_v$ matrix corresponds to $L, M, N, Fz, Fx$ channels, respectively (see $v_{INDI}$ in

https://doi.org/10.1017/aer.2023.87 Published online by Cambridge University Press

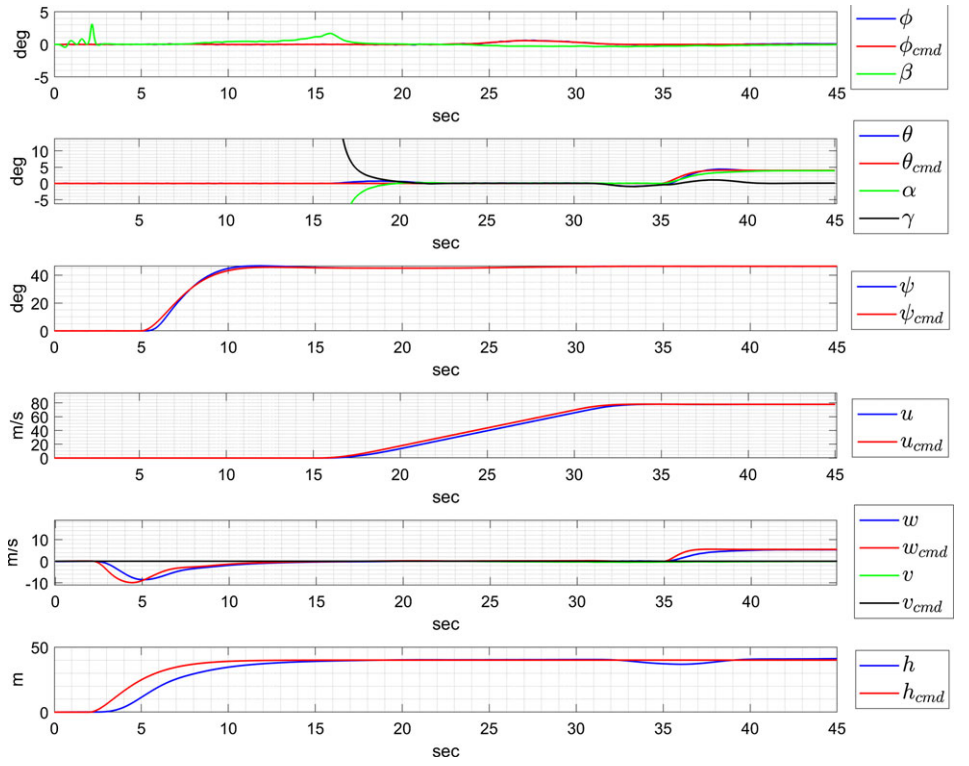


***Figure 6.*** *Simulation results for takeoff and transition from hover to cruise flight.*

Equation (12)). The weights of each channel are tuned using simulation results, and they can be fine-tuned easily for particular cases since each weight corresponds to one specific channel. Weights of $L$ and $M$ are higher since in case of actuator saturation the limited control authority is allocated to track the roll and pitch moment commands in the first place to guarantee stable flight. If the roll and pitch moment commands are tracked well, the remaining control authority is allocated to first tracking the yaw moment commands and then the force commands. With this prioritisation order, CA makes sure that the aircraft can track the moment commands in extreme flight conditions, such as multiple axis commands with severe disturbances or failures. To illustrate this case, assume that the aircraft is at hover condition. The pilot gives a strong climb command, and at this moment a severe roll moment disturbance (due to the wind/gust or failures) also occurs. However, due to the strong climb command, EDFs are very close to their maximum rpm and there is not enough thrust to handle roll moment disturbance. In other words, the controller's commands are out of actuator limits, and this leads to deficiency to handle roll disturbance. To resolve this problem, CA gives more priority to roll channel by allocating most of the remaining control authority to overcome the disturbance. This is an example case, but in most of the cases the first priority is always maintaining the stability in roll and pitch channels to avoid vital crashes. For specific cases, weights of $W_v$ can be adjusted to change the priority order. To conclude, CA has a major role in case of limited control authority. This case is simulated in Section 4.4, and it is observed that CA performance is highly critical and satisfactory. As mentioned, the first part of the cost function is related to the control minimisation. For the sake of simplicity, there is no aim to minimise specific control inputs. Therefore, $W_u$ matrix is chosen as $W_u = diag(1,\ 1,\ \ldots,\ 1)$, whereas the desired incremental control input is zero, i.e. $\Delta U_{des} = zeros\ (8, 1)$. Finally, the tuning parameter $\gamma$ is taken as 0.0001.

Since the INDI controller generates the incremental control input, the CA needs to be also formulated incrementally. Therefore, evaluation of the minimum and maximum actuator limits (i.e. $\Delta U_{CA,min}$ and

https://doi.org/10.1017/aer.2023.87 Published online by Cambridge University Press

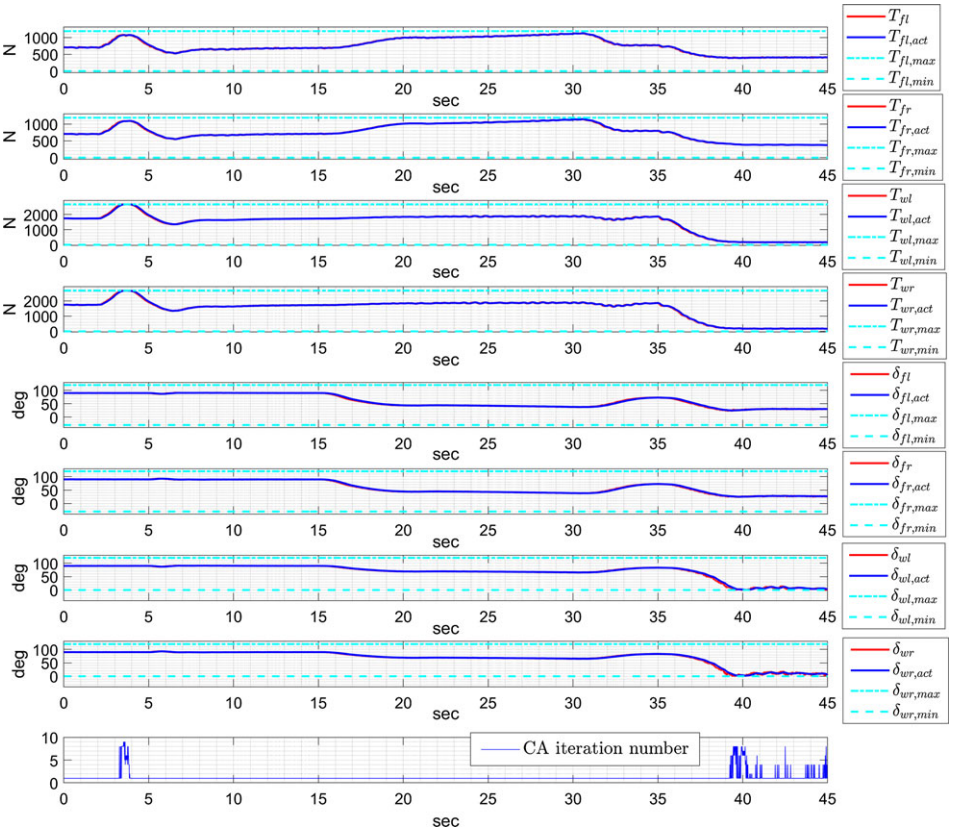


***Figure 7.*** *Simulation results for takeoff and transition from hover to cruise flight, actuator states.*

$\Delta U_{CA,max}$ in Equation (20)) at each time step is critical. Actuator limits are mapped from the physical control input ($U$) to the INDI control input ($U_{INDI}$) based on the thrust vector concept formulated in Equation (12). CA is adapted to the INDI controller formulation and the incremental limits are found as follows.

$$\left.\begin{aligned}
\Delta_{T_{x,min}} &= T_{x,min} - T_{x,act}, \quad with \quad T_{x,min} = sin(\pi/2 - \delta_{max})\sqrt{T_{x,act}^2 + T_{z,act}^2} \\
\Delta_{T_{z,min}} &= T_{z,min} - T_{z,act}, \quad with \quad T_{z,min} = cos(\pi/2 - \delta_{min})\sqrt{T_{x,act}^2 + T_{z,act}^2} \\
\Delta_{T_{x,max}} &= T_{x,max} - T_{x,act}, \quad with \quad T_{x,max} = \sqrt{T_{max}^2 - T_{z,act}^2} \\
\Delta_{T_{z,max}} &= T_{z,max} - T_{z,act}, \quad with \quad T_{z,max} = \sqrt{T_{max}^2 - T_{x,act}^2}
\end{aligned}\right\} \tag{21}$$

In the above equations, $\delta_{min}$, $T_{min}$ and $\delta_{max}$, $T_{max}$ are the minimum and maximum actuator limits defined in Table 4, and $T_{x,act}$, $T_{z,act}$ represent the x and z components of the thrust vector considering the actuator limits. Note that Equation (21) is given in generic form. It is calculated for each actuator state (i.e. front left, front right, wing left, wing right) specifically since limits are different (see Table 4).

In case of actuator limitations, the constrained optimisation problem is solved online at each time step within a sample time of 0.01 s. Therefore, the maximum number of iterations is set to 50 to limit the computational effort. Simulations are performed on a computer with a 1.8 GHz Intel core CPU. A detailed analysis is not made to check the required computational effort, but it is observed that the algorithm can be solved easily with the current computer technology. Detailed analysis of the active set algorithm's computational properties compared to the other approaches can be found in Ref. (45).

Another critical point is the continuity of the actuator commands when the CA becomes active/inactive. Based on the results given in Section 4, discontinuous actuator commands are not

https://doi.org/10.1017/aer.2023.87 Published online by Cambridge University Press

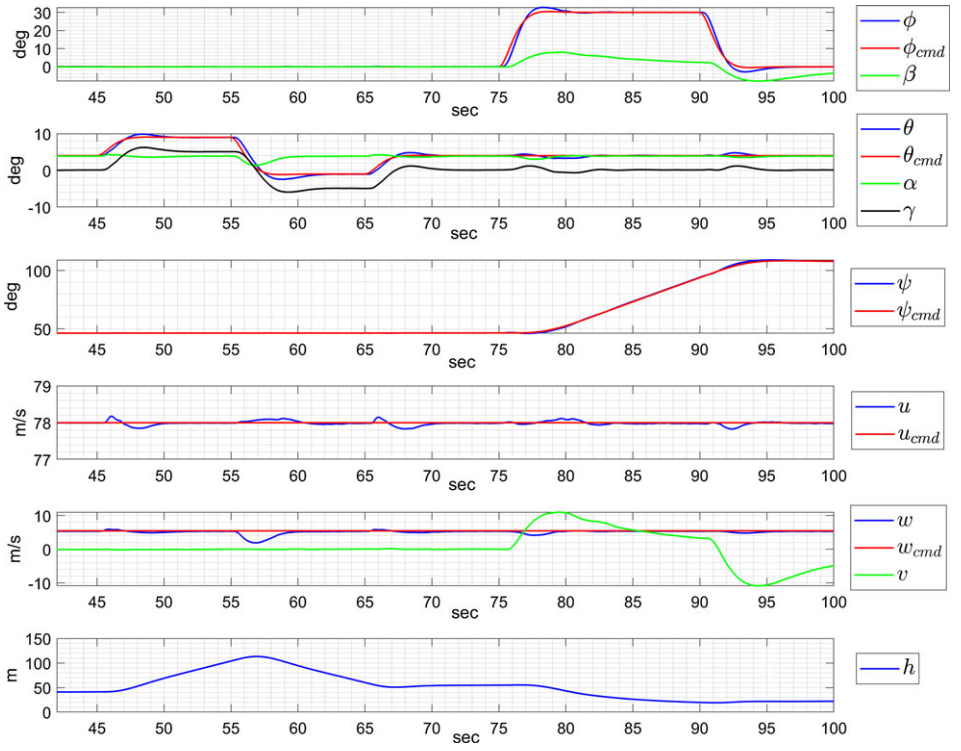


***Figure 8.*** *Simulation results for climbing/descending and coordinated turn at cruise.*

observed. At this point, it is reminded that the initial point of the CA algorithm is the output of the INDI controller (i.e. $\Delta U_{INDI}$). Moreover, $\Delta U_{INDI}$ of the overall INDI controller output given in Equation (17) is replaced with the output of CA algorithm $\Delta U_{CA}$ when CA algorithm is active (i.e. in case of actuator saturation), see Fig. 5.

Formulation of the unified INDI controller and integration of the CA method are described in this section. Performance of the overall controller is analysed in the next section via simulation results. A high-level block diagram of the closed loop simulation model is given in Fig. 5.

## 4.0 Simulation results

Simulations are performed to cover most of the flight envelope of the air taxi operation described previously. Results are given for four scenarios. In the first three scenarios (Sections 4.1, 4.2, and 4.3), the air taxi takeoff makes transitions between hover and forward flight, performs climb/descent and turns manoeuvers and land vertically. The aim is verification of the unified controller considering the wide flight envelope of the air taxi operation. Results show that the unified nonlinear controller works properly for the entire flight envelope without any modification for specific scenarios. In the last scenario (Section 4.4), the focus is testing the CA performance by injecting strong disturbances to the model. It is observed that CA performance is satisfactory, and without CA severe stability, problems occur in case of limited control authority. More detailed analysis of the INDI and CA performance are given in Ref. (27) including the robustness tests.

Results are given in two main plots, one shows the aircraft states and commands (with subscript *cmd*). The other shows the commanded ($T$ and $\delta$) and physically achieved ($T_{act}$ and $\delta_{act}$) actuator states. Before analysing the results, authors suggest to review the actuator states illustrated in Fig. 4 and defined in Section 3.1. The minimum ($T_{min}$ and $\delta_{min}$) and maximum ($T_{max}$ and $\delta_{max}$) actuator limits are also included

https://doi.org/10.1017/aer.2023.87 Published online by Cambridge University Press

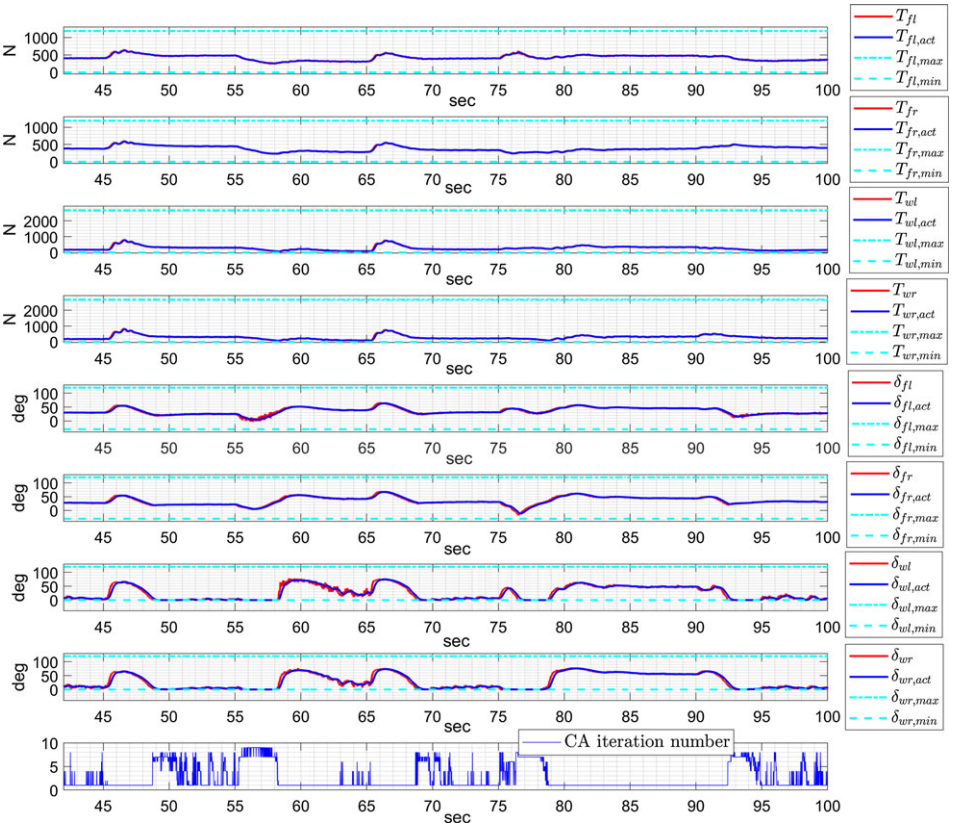


***Figure 9.*** *Simulation results for climbing/descending and coordinated turn at cruise, actuator states.*

into the figures to check whether the CA works properly and adjust the commands within the actuator limits. The CA iteration number is also given to observe the feasibility of the CA algorithm.

### *4.1 Takeoff & transition from hover to cruise flight*

As can be seen in Fig. 6, the altitude command is applied at 3 s. Thrust is increased on the front and wing sections while the flap angles are kept at 90° as expected (Fig. 7). A heading rate is applied at 5 s while the aircraft is gaining altitude. Very small changes in the flap angles are observed to track the heading command. This is due to the highly sufficient heading control authority at hover.

At 15 s, the aircraft reaches the desired altitude of 40 metres, and the speed command is applied between 15 and 35 s to perform the transition from hover to cruise flight. Aircraft gain speed by tilting the flaps to lower the flap angles and increase the thrust in body x-direction. Around 35 s, the desired cruise speed of 78 m/s is achieved. It is aimed to increase the angle-of-attack in cruise to take advantage of the aerodynamic lift. To achieve 4° cruise angle-of-attack, combined body velocity and pitch angle commands are applied between 35 and 40 s. A slight loss in altitude is observed during transients, but it is recovered at the steady state. The aircraft reaches the cruise trim condition with very small steady state errors.

According to Fig. 7, the CA becomes active frequently when the minimum thrust and flap angle limits are reached on the wing sections at cruise (i.e. after 40 s). The CA prioritises tracking roll and pitch moment commands over tracking yaw moment and force commands based on the weighting matrix $W_v$ defined in Equation (20). In this way, the limited control authority is adequately allocated to guarantee

https://doi.org/10.1017/aer.2023.87 Published online by Cambridge University Press

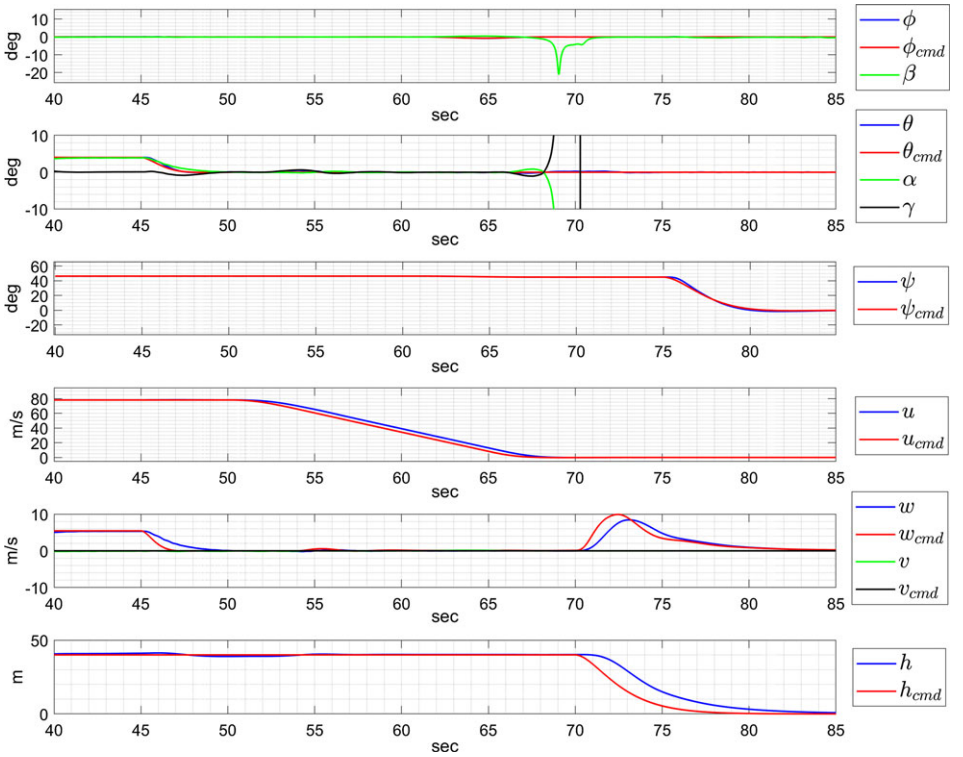


***Figure 10.*** *Simulation results for transition from cruise to hover flight and landing.*

stable flight in the first place. The same transition test is performed without activating the CA algorithm and purely commanding the INDI controller outputs to the actuators. It is seen that the INDI controller violates the actuator limits significantly when the combined pitch angle and body velocity commands are applied after 40 s. Without proper prioritisation (i.e. without the CA), the INDI controller can not satisfy stable flight in case of actuator saturation. In Section 4.4, a comparison test is performed at hover to show the importance of the CA algorithm in case of limited control authority.

### *4.2 Climbing/descending and coordinated turn at cruise*

As mentioned previously in Section 3.2.3, climbing/descending is achieved by adjusting the flight path angle via combined body velocity and pitch angle commands.

Based on Fig. 8, climb and descent manoeuvers are performed between 45 and 65 s by achieving positive and negative 5° flight path angles, respectively. Coordinated turn manoeuver is also tested at 75 s by applying 30° roll angle commands. Significant altitude loss is observed during the coordinated turns. This is an expected result since some of the total lift is used for turning. An outer loop controller can be designed to minimise the altitude loss similar to the one designed for hover (see $w_{cmd,nav,hover}$ in Equation (19)). The outer loop controller should increase total lift to overcome the lift deficiency during turns. In forward flight, this can be done by increasing angle-of-attack and/or airspeed. Some level of altitude loss might be inevitable due to the lack of control authority if bank angle is too high.

According to Fig. 9, actuator saturations are observed several times during these manoeuvers. The CA works as expected to guarantee stable flight with the prioritisation of moment channels. It is noted that the CA algorithm can find a solution with a maximum number of iteration less than 10.

https://doi.org/10.1017/aer.2023.87 Published online by Cambridge University Press

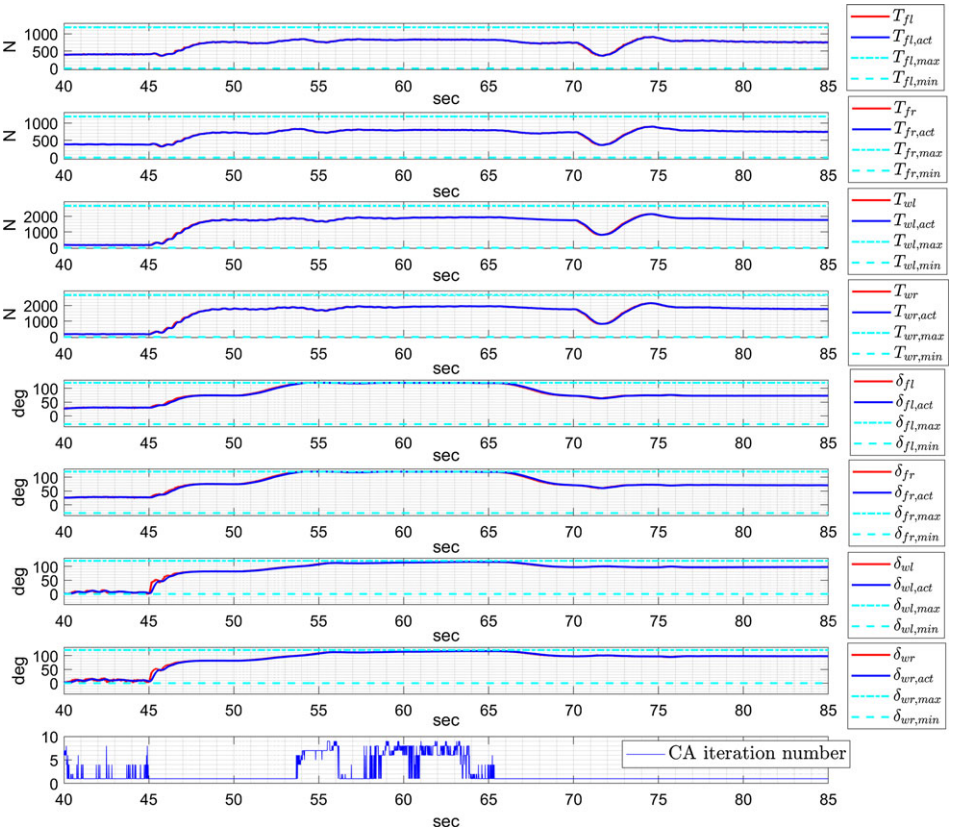


***Figure 11.*** *Simulation results for transition from cruise to hover flight and landing, actuator states.*

### *4.3 Transition from cruise to hover flight and landing*

Results of transition from cruise to hover flight and vertical landing are shown in Figs. 10 and 11. At 45 s, combined body velocity and pitch angle commands are applied to achieve zero angle-of-attack. The body x-velocity command is then applied between 50 and 70 s to achieve hover flight while keeping the altitude. Vertical landing is started at 70 s, and also aircraft heading is adjusted during the landing.

Based on Fig. 11, flap angles of both front and wing sections reach maximum limits during the transition to decelerate the aircraft. Therefore, the CA becomes active many times to prioritise moment commands over force commands. This is an expected result considering the significant deceleration command during the cruise to hover transition.

### *4.4 Importance of the CA: severe roll moment disturbance at hover*

As mentioned previously, the CA has a very crucial role in case of actuator saturation. To show the CA's effectiveness, a test case is simulated when the CA is on (i.e. INDI+CA) and off (i.e. only the INDI controller). As shown in Fig. 12, a strong roll moment disturbance is applied at hover (at 3 s) for both conditions (i.e. CA ON and CA OFF). Simultaneously, the pilot wants to gain altitude and apply body z-velocity command ($w_{cmd}$).

According to Fig. 13, thrust authority is not enough to track the pilot command and reject the roll disturbance at the same time. The INDI controller generates thrust commands above the maximum physical limits (see dashed and red lines in Fig. 13). Therefore, disturbance rejection properties are not as desired due to the saturation related discrepancy between the commanded and physically achieved

https://doi.org/10.1017/aer.2023.87 Published online by Cambridge University Press

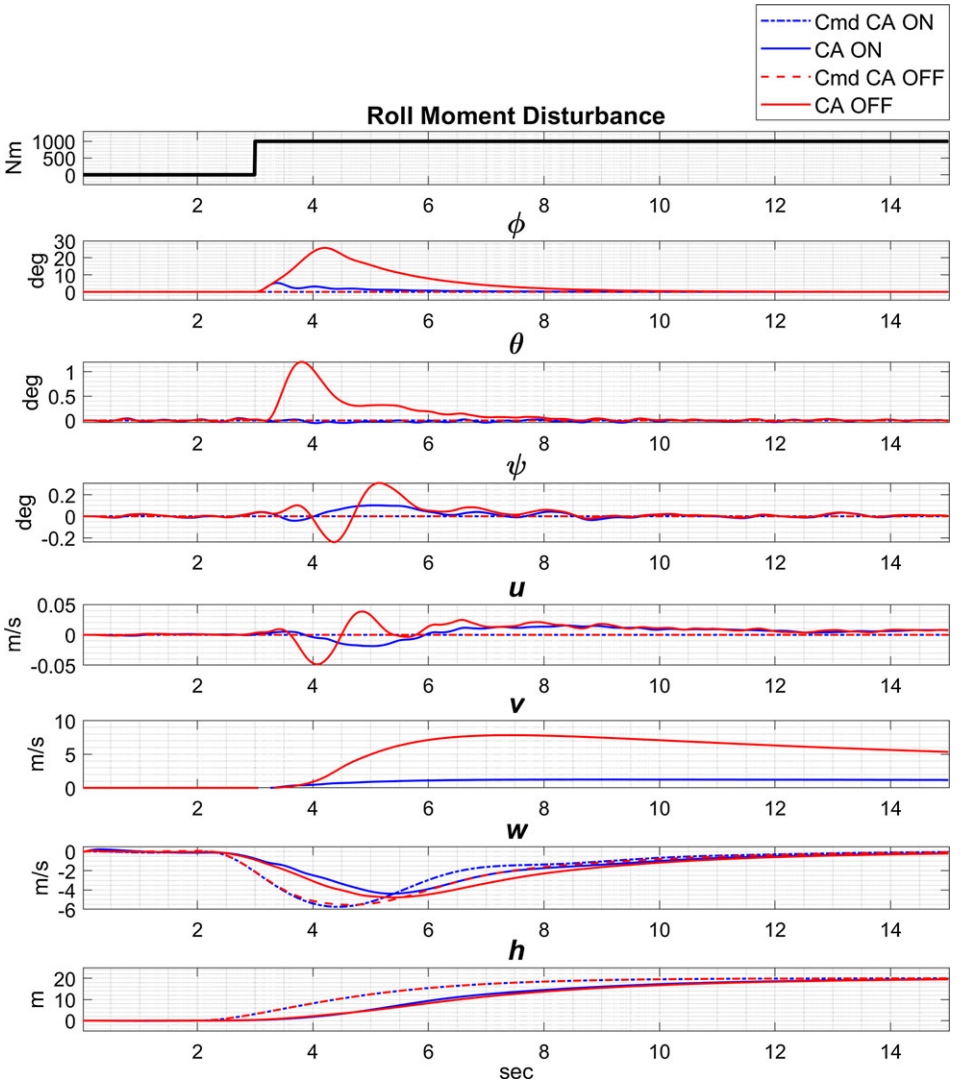


***Figure 12.*** *Comparative simulation results that shows the importance of the CA.*

actuator states. When CA is OFF, approximately 25° roll angle is observed due to the disturbance (Fig. 13).

However, when the CA is active, disturbance rejection properties are much better since the CA prioritises the moment commands over the force commands considering the actuator saturation. There is no discrepancy between the physically achieved and commanded thrust when the CA is on (see dashed and blue lines in Fig. 13). The trade-off is the worse tracking of the body z-velocity command, as seen in the *w* plot of Fig. 12. The deteriorated tracking performance of the body z-velocity command can be accepted since allocating the limited control authority to the moment channels is more important regarding the stability. When CA is ON, roll moment disturbance only cause 7–8 deg roll angle, which is much less than the case when CA is OFF (Fig. 12).

To conclude, CA performs very well and allocates the limited control authority properly to guarantee stable flight in case of severe disturbance. More detailed analysis of the CA performance are given in Ref. (27).

https://doi.org/10.1017/aer.2023.87 Published online by Cambridge University Press

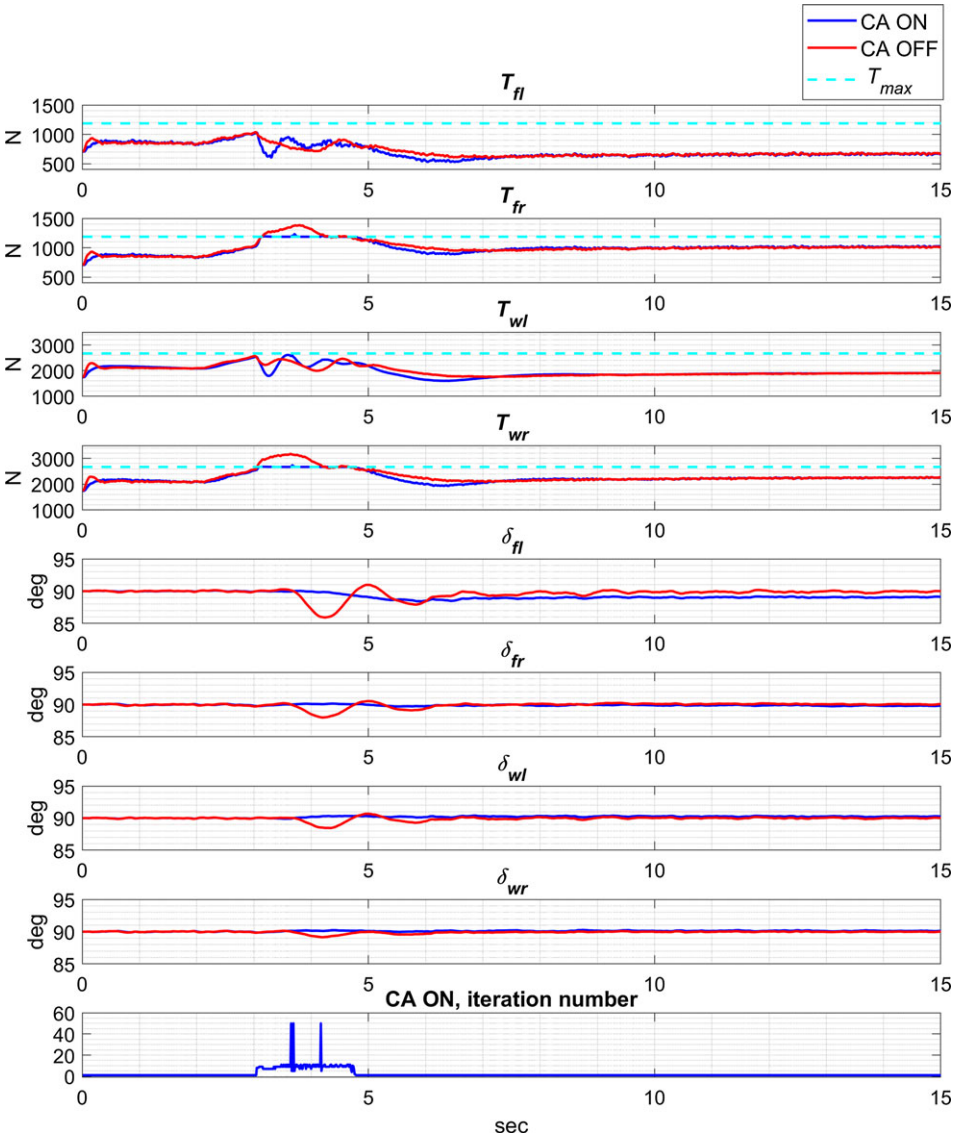


***Figure 13.*** *Comparative simulation results that shows the importance of the CA, actuator states.*

## 5.0 Conclusion

This study focuses on defining and solving flight control problems of a novel fixed wing eVTOL air taxi considering the wide flight envelope. First, the preliminary flight dynamics model of the air taxi is generated separately for the low-speed hover and high-speed forward flight. Transition dynamics are modeled by simply merging the hover and forward flight models based on the airspeed. Control of the air taxi is achieved by adjusting the thrust vector of numerous EDFs distributed over the front and wing sections, and modeling of the EDFs/propulsion dynamics is based on the datasheet of a commercially used product. The air taxi modeled in this paper does not have any conventional control and stability surfaces which differentiates it from the other fixed-wing eVTOLs studied in literature. Not having conventional control/stability surfaces has significant advantages such as improved aerodynamic efficiency, simplicity in design, better sizing/mass reduction, etc. However, it also comes with problems regarding

https://doi.org/10.1017/aer.2023.87 Published online by Cambridge University Press

the flight control described throughout the paper (e.g. open-loop directional unstability, limited control authority at specific flight conditions, resolving actuator saturation is not straightforward due to thrust vector couplings, etc.).

As described in the introduction part, two central challenges regarding the flight controller design are the severe nonlinearities/couplings that emerge in the transition regions and the problems related to the over-actuation and limited control authority (i.e. actuator saturation) for specific flight conditions. An INDI-based controller is designed to solve the first problem, and a CA method is integrated into the INDI controller to mitigate the adverse effects of the actuator saturation. INDI is the incremental version of the NDI, and it performs the dynamic inversion based on the sensor data instead of the aircraft model. The INDI approach's main advantage is reduced dependency on the aircraft model during the inversion, making it the right candidate considering the described challenges.

On the other hand, the INDI-based controller becomes more sensitive to sensor noise and delay. Considering this point, gyroscope and accelerometer models are included in the model based on a MEMS IMU sensor data, and second-order linear filters are used to reduce noise levels. The INDI controller is formulated effectively to resolve the coupling related problems of the thrust vector control concept. The overall INDI-based design aims to have an unified nonlinear controller that covers the entire flight envelope. In addition to that, an optimisation based CA method is designed and integrated into the INDI controller considering the incremental nature of the INDI formulation and coupled pure thrust vector control. The CA prioritises the rotational control over the translational control when actuator position limits are reached. Simulations are performed to test the overall controller for the entire flight envelope. The controller shows satisfactory performance, also considering the disturbance rejection properties. Results illustrate that the CA plays a vital role in the presence of actuator saturation, and stable flight can not be achieved without proper allocation of the limited control authority. Further studies can focus on the robustness to sensor model (i.e. sensor noise and delay), considering that INDI is a sensor-based control approach. Moreover, the CA design could be extended to consider also rate limitations of the actuators.

## References

[1] Moore, M.D. The third wave of aeronautics: On-demand mobility, *SAE Techn. Paper Ser., SAE Trans.*, 2006, pp 713–722. https://doi.org/10.4271/2006-01-2429

[2] Holden, J. and Goel, N. Uber elevate: Fast-forwarding to a future of on-demand urban air transportation, Uber Inc., San Francisco, CA, 2016.

[3] Moore, M.D. and Fredericks, B. Misconceptions of electric aircraft and their emerging aviation markets, *52nd Aerosp. Sci. Meeting*, 2014, p 0535. https://doi.org/10.2514/6.2014-0535

[4] Gohardani, A.S., Doulgeris, G. and Singh, R. Challenges of future aircraft propulsion: A review of distributed propulsion technology and its potential application for the all electric commercial aircraft, *Progr. Aerosp. Sci.*, **47**, (5), 2011, pp 369–391. https://doi.org/10.1016/j.paerosci.2010.09.001

[5] Kreimeier, M., Strathoff, P., Gottschalk, D. and Stumpf, E. Economic assessment of air mobility on-demand concepts, *J. Air Transport.*, **26**, (1), 2018, pp 23–36. https://doi.org/10.2514/1.D0058

[6] Kim, H.D., Perry, A.T. and Ansell, P.J. A review of distributed electric propulsion concepts for air vehicle technology, *2018 AIAA/IEEE Electric Aircraft Technologies Symposium (EATS)*, IEEE, 2018, pp 1–21. https://doi.org/10.2514/6.2018-4998

[7] Niemiec, R., Gandhi, F. and Singh, R. Control and performance of a reconfigurable multicopter, *J. Aircr.*, **55**, (5), 2018, pp 1855–1866. https://doi.org/10.2514/1.C034731

[8] Ma, Y., Zhang, W., Zhang, Y., Zhang, X. and Zhong, Y. Sizing method and sensitivity analysis for distributed electric propulsion aircraft, *J. Aircr.*, **57**, (4), 2020, pp 730–741. https://doi.org/10.2514/1.C035581

[9] Stoll, A.M., Stilson, E.V., Bevirt, J. and Pei, P.P. Conceptual design of the Joby S2 electric VTOL PAV, *14th AIAA Aviation Technology, Integration, and Operations Conference*, 2014, p 2407. https://doi.org/10.2514/6.2014-2407

[10] Finger, D.F., Braun, C. and Bil, C. A review of configuration design for distributed propulsion transitioning VTOL aircraft, *Asia-Pacific International Symposium on Aerospace Technology-APISAT*, Korean Soc. for Aeronautical and Space Sciences Seoul, Korea, 2017, pp 3–5.

[11] Lilium GmbH, 2023, https://lilium.com/. Accessed on 11 July 2023.

[12] Di Francesco, G. and Mattei, M. Modeling and incremental nonlinear dynamic inversion control of a novel unmanned tiltrotor, *J. Aircr.*, **53**, (1), 2016, pp 73–86. https://doi.org/10.2514/1.C033183

https://doi.org/10.1017/aer.2023.87 Published online by Cambridge University Press

[13] Lombaerts, T., Kaneshige, J., Schuet, S., Aponso, B.L., Shish, K.H. and Hardy, G. Dynamic inversion based full envelope flight control for an eVTOL vehicle using a unified framework, *AIAA Scitech 2020 Forum*, 2020, p 1619. https://doi.org/10.2514/6.2020-1619
[14] Yang, H., and Morales, R., "Robust full-envelope flight control design for an eVTOL vehicle," *AIAA Scitech 2021 Forum*, 2021, p. 0254.
[15] Willis, J.B. and Beard, R.W. Pitch and thrust allocation for full-flight-regime control of winged eVTOL UAVs, *IEEE Control Syst. Lett.*, **6**, 2021, pp 1058–1063.
[16] Digital DATCOM, Wikipedia, 2023, https://en.wikipedia.org/wiki/United_States_Air_Force_Stability_and_Control_Digital_DATCOM. Accessed 01 August 2023.
[17] Schuebeler DS-215-DIA HST Electric Ducted Fan Datasheet, Schuebeler-jets, 2021, https://www.schuebeler-jets.de/en/products/hst-en. Accessed 18 June 2021.
[18] Rosema, C., Doyle, J., Auman, L., Underwood, M. and Blake, W.B. Missile DATCOM user's manual–2011 revision, *Air Force Reseach Laboratory Report AFRL-RB-WP-TR-2011-3071*, 2011.
[19] Roskam, J. *Airplane Design: Preliminary Calculation of Aerodynamic, Thrust and Power Characteristics*, Roskam Aviation and Engineering Corporation, 1985.
[20] Roskam, J. *Airplane Flight Dynamics and Automatic Flight Controls*, DARcorporation, 1995.
[21] Sooy, T.J. and Schmidt, R.Z. Aerodynamic predictions, comparisons, and validations using missile datcom (97) and aeroprediction 98 (ap98), *J. Spacecr. Rockets*, **42**, (2), 2005, pp 257–265.
[22] Abney, E. and McDaniel, M. High angle of attack aerodynamic predictions using missile datcom, *23rd AIAA Applied Aerodynamics Conference*, 2005, p 5086.
[23] Vasile, J.D., Bryson, J. and Fresconi, F. Aerodynamic design optimization of long range projectiles using missile DATCOM, *AIAA Scitech 2020 Forum*, 2020, p 1762.
[24] Segui, M., Mantilla, M. and Botez, R.M. Design and validation of an aerodynamic model of the cessna citation x horizontal stabilizer using both OpenVSP and digital Datcom, *Int. J. Aerosp. Mech. Eng.*, **12**, (1), 2018, pp 45–53.
[25] Doyle, J. and Rosema, C. Improved validation methodology for missile DATCOM development, *49th AIAA Aerospace Sciences Meeting including the New Horizons Forum and Aerospace Exposition*, 2011, p 1241.
[26] McLean, D. *Automatic Flight Control Systems*, Prentice Hall, Englewood Cliffs, NJ, 1990.
[27] Suicmez, E.C. Full envelope nonlinear controller design for a novel Electric VTOL (eVTOL) Air-taxi via INDI Approach Combined with CA, Ph.D. thesis, Middle East Technical University, 2021.
[28] Lombaerts, T., Kaneshige, J., Schuet, S., Hardy, G., Aponso, B.L. and Shish, K.H. Nonlinear dynamic inversion based attitude control for a hovering quad tiltrotor eVTOL vehicle, *AIAA Scitech 2019 Forum*, 2019, p 0134. https://doi.org/10.2514/6.2019-0134
[29] Prasuhn, A.L. *Fundamentals of Fluid Mechanics*, Prentice Hall, 1980.
[30] Freeman, J. Methodology for distributed electric propulsion aircraft control development with simulation and flight demonstration. OpenVsp, 2021, http://openvsp.org/wiki/lib/exe/fetch.php?media=workshop17:esaero-uiuc_nasa_sttr.pdf. Accessed 18 June 2021.
[31] Freeman, J.L. and Klunk, G.T. Dynamic flight simulation of spanwise distributed electric propulsion for directional control authority, *2018 AIAA/IEEE Electric Aircraft Technologies Symposium (EATS)*, IEEE, 2018, pp 1–15. https://doi.org/10.2514/6.2018-4997
[32] Smith, P. A simplified approach to nonlinear dynamic inversion based flight control, *23rd Atmospheric Flight Mechanics Conference*, 1998, p 4461. https://doi.org/10.2514/6.1998-4461
[33] Bacon, B. and Ostroff, A. Reconfigurable flight control using nonlinear dynamic inversion with a special accelerometer implementation, *AIAA Guidance, Navigation, and Control Conference and Exhibit*, 2000, p 4565. https://doi.org/10.2514/6.2000-4565
[34] Enns, D., Bugajski, D., Hendrick, R. and Stein, G. Dynamic inversion: an evolving methodology for flight control design, *Int. J. Control*, **59**, (1), 1994, pp 71–91. https://doi.org/10.1080/00207179408923070
[35] Smeur, E.J., Chu, Q. and de Croon, G.C. Adaptive incremental nonlinear dynamic inversion for attitude control of micro air vehicles, *J. Guid. Control Dynam.*, **39**, (3), 2016, pp 450–461. https://doi.org/10.2514/1.G001490
[36] Sieberling, S., Chu, Q. and Mulder, J. Robust flight control using incremental nonlinear dynamic inversion and angular acceleration prediction, *J. Guid. Control Dynam.*, **33**, (6), 2010, pp 1732–1742. https://doi.org/10.2514/1.49978
[37] Chen, H.B. and Zhang, S.G. Robust dynamic inversion flight control law design, *2nd International Symposium on Systems and Control in Aerospace and Astronautics*, IEEE, 2008, pp 1–6. https://doi.org/10.1109/ISSCAA.2008.4776382
[38] Wang, X., Van Kampen, E.-J., Chu, Q. and Lu, P. Stability analysis for incremental nonlinear dynamic inversion control, *J. Guid. Control Dynam.*, **42**, (5), 2019, pp 1116–1129. https://doi.org/10.2514/1.G003791
[39] Pollack, T., Looye, G. and Van der Linden, F. Design and flight testing of flight control laws integrating incremental nonlinear dynamic inversion and servo current control, *AIAA Scitech 2019 Forum*, 2019, p 0130. https://doi.org/10.2514/6.2019-0130
[40] Smeur, E.J., de Croon, G.C. and Chu, Q. Cascaded incremental nonlinear dynamic inversion for MAV disturbance rejection, *Control Eng. Pract.*, Vol. **73**, 2018, pp. 79–90. https://doi.org/10.1016/j.conengprac.2018.01.003
[41] Durham, W., Bordignon, K.A. and Beck, R. *Aircraft Control Allocation*, John Wiley & Sons, 2017.
[42] Bodson, M. Evaluation of optimization methods for control allocation, *J. Guid. Control Dynam.*, **25**, (4), 2002, pp 703–711. https://doi.org/10.2514/2.4937
[43] Oppenheimer, M.W., Doman, D.B. and Bolender, M.A. Control allocation for over-actuated systems, *14th Mediterranean Conference on Control and Automation*, IEEE, 2006, pp. 1–6. https://doi.org/10.1109/MED.2006.328750

https://doi.org/10.1017/aer.2023.87 Published online by Cambridge University Press

[44] Johansen, T.A. and Fossen, T.I. Control allocation—A survey, *Automatica*, **49**, (5), 2013, pp 1087–1103. https://doi.org/10.1016/j.automatica.2013.01.035
[45] Harkegard, O. Efficient active set algorithms for solving constrained least squares problems in aircraft control allocation, *Proceedings of the 41st IEEE Conference on Decision and Control*, Vol. 2, IEEE, 2002, pp 1295–1300. https://doi.org/10.1109/CDC.2002.1184694
[46] Stevens, B.L., Lewis, F.L. and Johnson, E.N. *Aircraft Control and Simulation: Dynamics, Controls Design, and Autonomous Systems*, John Wiley & Sons, 2015.
[47] Barreda Pupo, L. Characterization of errors and noises in MEMS inertial sensors using Allan variance method, Master's thesis, Universitat Politècnica de Catalunya, 2016.

**Cite this article:** Suiçmez E.C. and Kutay A.T. Full envelope nonlinear flight controller design for a novel electric VTOL (eVTOL) air taxi. *The Aeronautical Journal*, https://doi.org/10.1017/aer.2023.87